APPLICATION OF THE THREE SHORT CALIBRATION TECHNIQUE IN A LOW
FREQUENCY FOCUS BEAM SYSTEM

THESIS

William E. Gunn, Jr, Second Lieutenant, USAF

AFIT/GE/ENG/10-10

DEPARTMENT OF THE AIR FORCE
AIR UNIVERSITY

AIR FORCE INSTITUTE OF TECHNOLOGY

Wright-Patterson Air Force Base, Ohio

AFIT/GE/ENG/10-10

APPLICATION OF THE THREE SHORT CALIBRATION TECHNIQUE IN A
LOW FREQUENCY FOCUS BEAM SYSTEM

THESIS

Presented to the Faculty

Department of Electrical and Computer Engineering

Graduate School of Engineering and Management

Air Force Institute of Technology

Air University

Air Education and Training Command

In Partial Fulfillment of the Requirements for the

Degree of Master of Science in Electrical Engineering

William E. Gunn, Jr, B.S.E.E.

Second Lieutenant, USAF

March 2010

AFIT/GE/ENG/10-10

APPLICATION OF THE THREE SHORT CALIBRATION TECHNIQUE IN A LOW FREQUENCY FOCUS BEAM SYSTEM

William E. Gunn, Jr, B.S.E.E.

Second Lieutenant, USAF

Approved:

Michael Havrilla

Dr. Michael J. Havrilla (Chairman)

16 Mar 2010

date

Mike a Saville

Maj Michael A. Saville PhD (Member)

16 Mar 2010

date

[signature]
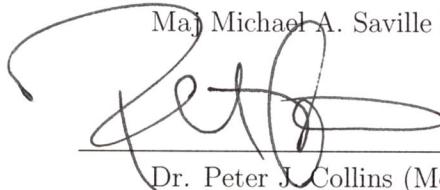
Dr. Peter J. Collins (Member)

16 MAR 2010

date

AFIT/GE/ENG/10-10

Abstract

Electromagnetic material characterization is the process of determining the constitutive parameters of matter. In simple media, these parameters are permittivity and permeability. Characterization of these values is often accomplished through the use of waveguides, transmission lines, coaxial cables, and resonant cavities. Free space measurements systems are employed since they are non destructive (i.e., no sample machining is required) and broadband. Traditionally, time domain gating is utilized to mitigate systematic errors. However, an artifact of this calibration technique is band edge corruption due to data windowing. The goal of this research is to develop and apply a Three Short Calibration Technique to the General Electric Low Frequency (0.5-2GHz) Focus Beam System in order to preserve band edge data. It is shown that when working with low frequencies, such as the focus of this research, coupling effects due to multiple bounces within the collimating and focusing lenses as well as lens-sample interaction are not easily calibrated out. Although the coupling effects introduce extraneous clutter into the extracted constitutive parameter values, the results obtained agree with the known reference values of tested dielectric samples. It is concluded that with a more in depth study in sample/lens interaction at low frequencies, this calibration technique could prove useful in the accurate extraction of the desired low frequency constitutive parameter values.

Acknowledgements

First and foremost, I owe a large debt of gratitude to GOD. With him and through him ALL things are possible. It is by his GRACE that I have made it through this period of academic growth.

To my advisor Dr. Michael Havrilla, thank you for all of your support and your unprecedented passion for teaching. Your drive to broaden a student's mind by emphasizing the intimacy involved between mathematics and physics is truly inspirational. Thank you for showing me the mountains that I can reach.

To my committee members, Dr. Peter Collins and Major Michael Saville, thank you for your time, support, technical expertise, and suggestions into making this thesis something that I can truly call an accomplishment.

To my Mom and Dad, thank you for instilling upon me that "Never Quit" attitude. You never let me settle for anything other than my best effort. It is through your inspiration that I have become the man that I am today. I LOVE you both. The solid foundation that you built for me to stand on has allowed me to comfortably stretch and reach for the stars.

Lastly I would like to thank my sister, you were deployed during my high school and undergrad graduation ceremonies, this Thesis is dedicated to you. Watching you accomplish so much growing up as a child FORCED me to be GREAT. You have been a huge inspiration in my life and I'm glad you will be here to see me walk across the stage.

William E. Gunn, Jr

Table of Contents

List of Figures

List of Tables

APPLICATION OF THE THREE SHORT CALIBRATION TECHNIQUE IN A

LOW FREQUENCY FOCUS BEAM SYSTEM

I. Introduction

The measurement of a sample's constitutive parameters is of great interest to engineers as it allows for the accurate prediction of how electromagnetic waves will interact with a particular material. Evaluation of the complex permittivity and permeability is required not only for engineering but also industrial applications. Numerous material characterization techniques exist, each with particular advantages and disadvantages. There is no single optimum technique for all material characterizations. In trying to characterize low observable materials, traditional methods such as waveguides, transmission lines, co-axial cables, and resonant cavities tend to introduce error due to inhomogeneities, air gaps, and finite conductivity that are difficult to correct. Free-space techniques, such as the focus beam system, offer an advantage for characterization when dealing with these types of materials since they are broadband and nondestructive.

1.1   Problem Statement

An automated network analyzer system is used to make frequency swept S-parameter measurements on the focused-beam sample fixture from which complex permittivity and permeability may be calculated. However, before any measurements can be taken the NWA must first be calibrated.

Automated network analyzers inherently have many errors associated with the measured scattering parameters. The sources for these errors according to [1] are

- Imperfect connector matching

- Imperfect calibration standards

- Nonlinearity of mixers

- Gain and phase drifts in IF amplifiers

- Noise introduced by the analog to digital converter

- Imperfect tracking in dual-channel systems

Calibrating the NWA attempts to remove the systematic uncertainties by measuring a set of known standards. After calibration, the NWA operates with error correction and automatically updates the measurements with the calibration information. The complex material parameters can then be computed from the measured scattering parameters using a computational algorithm such as the Nicolson-Ross-Weir (NRW) or Newton-Raphson Root Search techniques [12, 20].

The Low Frequency Focus Beam System at General Electric currently uses a time domain gating technique in order to obtain calibrated S-Parameter measurements which subsequently leads to the extraction of material constitutive parameters. The problem with this method is that critical data is attenuated in the high and low frequency region (i.e. band edge data) due to data windowing. General Electric is interested in preserving the data that is lost through this process, especially at the low end of the frequency band. The three short calibration technique aims to be an effective way of fully calibrating this system, so that the time domain gating method may be avoided [18].

1.2   Limitations

The three short calibration technique is band limited due to degeneracy of shorts spaced greater than or equal to a half wavelength. Special care must be taken in the derivation of the maximum spacing constraint between the shorts. This will be accomplished by establishing a set bandwidth for the experiment (0.5-2GHz).

General Electric uses a mechanical mechanism to reposition the sample holder. Although this is an extremely good idea, accurate precision may prove to be an issue as a high degree of accuracy when translating from position to position is needed in order to not introduce phase errors in the extracted data. It will also be important to see

if this change in phase can be resolvable. There are also other errors associated with measurements in the low frequency regime, including lower signal levels embedded in low frequency clutter, coupling effects, and antenna/lens internal reflections. The three short calibration technique investigated in this research seeks to mitigate these errors.

1.3 Scope

The three short calibration technique will be applied to the Low Frequency Focus Beam System. As previously discussed, this calibration technique is band limited. Communication with the engineers at General Electric established an interest in the bandwidth between 500Mhz and 2GHz. Two dielectrics will be tested for validation, a fiberglass panel and a sheet of plexiglas. The current technique of time domain gating will be used on the fiberglass panel to establish a comparison of data with the full frequency domain calibration results. An analysis of post calibration error will be discussed.

1.4 Thesis Organization

This thesis is divided into five chapters. Chapter two provides a brief description of permittivity and permeability. Current calibration techniques used on similar Free Space measurement systems will be discussed and pros and cons will be reviewed. A section on the time domain gating technique will also be reviewed to increase knowledge in the need for an alternative calibration technique for this system. Chapter three provides an overview of the NWA 12-term error model, since the 3-short calibration technique is used to calculate these error terms. The maximum short-spacing constraint is established and a verification of phase angle resolution is performed. Chapter four discusses the results of the experimental measurements as well as speculation on any error still present after application of the calibration technique. Chapter five will give a conclusion to all results found in this thesis. It will also suggest changes to the experimental setup that can be made to possibly enhance accuracy.

II. Literature Review and Background Material

In order to understand the importance of measuring the constitutive parameters of materials, or even the reason behind taking an interest in developing multiple techniques in doing so, one must strive to develop a fundamental understanding in certain key areas involved in the field of electromagnetics. This chapter will focus on background concepts that will bring out theory and solidify the justification of why the "three short calibration technique" can be applicable to the focus beam system.

2.1 Properties of Matter

Materials are typically defined and described by their constitutive parameters. The main purpose of most material measurements is to ultimately obtain data that will allow for calculation of the material's permittivity and/or permeability values. These values are known as a material's constitutive parameters. There is no method to date that allows for the direct measurement of a material's constitutive parameters, these values are calculated through various novel numerical and iterative techniques, each having their own advantages and disadvantages. Once a material's constitutive parameters have been extracted, fairly accurate prediction of how the material will react when an electromagnetic wave becomes incident upon it can be determined. This information is of importance in the engineering community because it allows for engineers to place layers upon perfect electrical conductors (PECs), for example, in an effort to control electromagnetic scattering.

A further discussion of permittivity and permeability is needed in order to understand the big picture of going through the trouble of extracting these values. In order to develop these definitions a discussion on the physical structure of matter will be presented. A review of these topics will enhance the understanding of the various methods for extracting the constitutive values of materials, and ultimately the understanding of the importance of advancing the calibration procedure for the Low Frequency Focus Beam System. This thesis involves the application of a calibration technique on a system that will be utilized to measure the scattering matrix of a
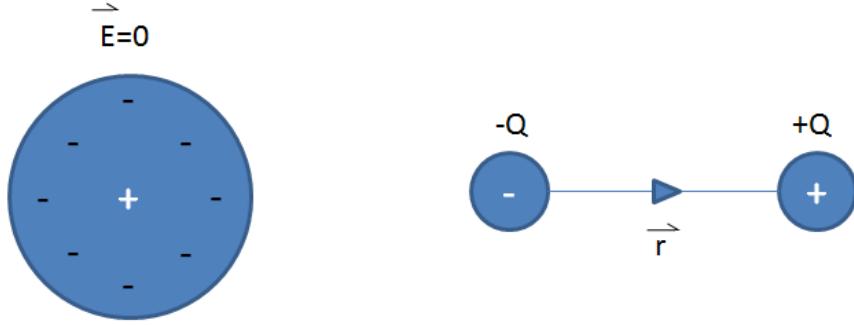
Figure 2.1:   Polarization of a nonpolar atom or molecule.

device under test. This scattering matrix will in turn be mathematically manipulated in order to extract permittivity and permeability values of the sample of interest.

2.2   Dielectrics

Following a development in [21], a concise derivation of the dielectric constant is presented. In order to break down the structure of a dielectric, its atom will be depicted by a negative charge $-Q$ (electron cloud) and a positive charge $+Q$ (nucleus). The nuclei will represent point charges and the electron cloud consisting of multiple negative charges. There is assumed to be an equal amount of positive and negative charges, making the atom electrically neutral. When an electric field $\vec{E}$ is incident upon this atom, the negative charge is displaced from its equilibrium position as shown in Figure 2.1. The result of these actions is the creation of a dipole, and the dielectric becomes polarized with dipole moment

$$\vec{p} = Q\vec{r} \tag{2.1}$$

where $\vec{r}$ is the distance vector from $-Q$ to $+Q$. This is depicted in figure 2.1. If there are N dipoles within a volume δv of the dielectric, the total dipole moment due to the electric field becomes

$$Q_1\vec{r_1} + Q_2\vec{r_2} + ... + Q_N\vec{r_N} = \sum_{k=1}^{N} Q_k\vec{r_k}. \tag{2.2}$$

5

The density of these dipole moments therefore can be expressed as

$$\vec{P} = \lim_{\Delta v \to 0} \frac{\sum_{k=1}^{N} Q_k \vec{r}_k}{\Delta v}. \tag{2.3}$$

The major effect of $\vec{E}$ on a dielectric is the creation of dipole moments in the direction of $\vec{E}$. The behavior previously described is that of a nonpolar dielectric. Dielectrics with built in permanent dipoles that are randomly oriented are called polar dielectrics. When these types of dielectrics are in the presence of $\vec{E}$, their dipoles align themselves with $\vec{E}$, leading to a net polarization density of $\vec{p}$.

When applying $\vec{E}$ to a dielectric material, the electric flux density $\vec{D}$ is greater than it would be in free space. This is defined by the relation

$$\vec{D} = \epsilon_0 \vec{E} + \vec{P}. \tag{2.4}$$

If a material is linear and isotropic, the polarization will be proportional to the applied electric field, thus

$$\vec{p} = \chi_e \epsilon_0 \vec{E} \tag{2.5}$$

where χ_e is the electric susceptibility of the material. By substituting equation 2.5 into equation 2.4, one can now define D to be

$$\vec{D} = \epsilon \vec{E} \tag{2.6}$$

where

$$\epsilon = \epsilon_0 \epsilon_r \tag{2.7}$$

and

$$\epsilon_r = 1 + \chi_e = \frac{\epsilon}{\epsilon_0}. \tag{2.8}$$
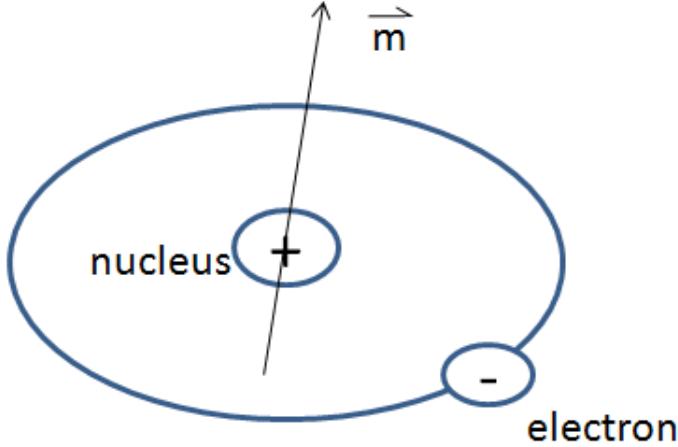
Figure 2.2:   Electron orbiting around the nucleus

The parameter ϵ is said to be the permittivity of the dielectric, ϵ_0 is the permittivity of free space having value

$$\epsilon_0 \approx 8.854 \times 10^{-12} \frac{F}{m}, \tag{2.9}$$

and ϵ_r is the dielectric constant or relative permittivity.

2.3   Magnetics

A similar development presented in [21] will be followed for the description of relative permeability. In parallel with the development of polarization, electrons also rotate about their own nucleus. The act of an electron orbiting around the nucleus creates a magnetic dipole $\vec{m}$ as illustrated in figure 2.2.

Without the presence of an external $\vec{B}$ field, the sum of magnetic moments $\vec{m}$ for many materials is zero due to random orientation. This phenomena is depicted in Figure 2.3. In the presence of an external B field, the magnetic moments leading to the magnetization density

$$\vec{M} = \frac{\lim\limits_{\Delta v \to 0} \sum\limits_{k=1}^{N} \vec{m}_k}{\Delta v} \tag{2.10}$$
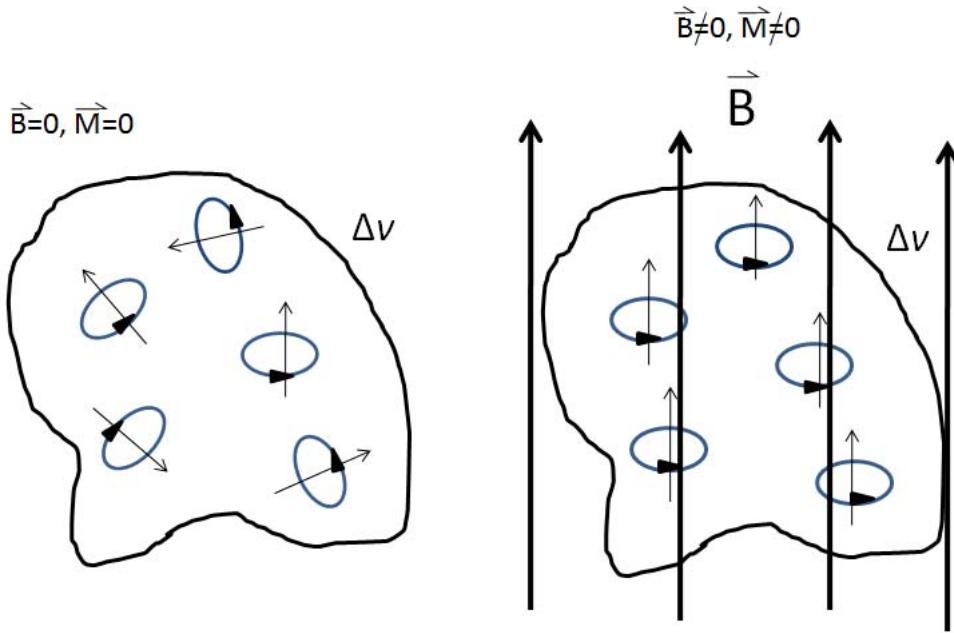
Figure 2.3:   Magnetic dipole moment before and after $\vec{B}$ is applied.

Similar to $\vec{D}$, an auxilliary fied $\vec{H}$ is defined to accommodate the effects of the magnetization density, namely,

$$\vec{H} = \frac{\vec{B}}{\mu_0} \tag{2.11}$$

or

$$\vec{B} = \mu_0(\vec{H} + \mu_0) \tag{2.12}$$

, where $\vec{H}$ is the magnetic field intensity.

Equation 2.12 holds for all materials whether they are linear or not. For linear materials, $\vec{M}$ depends linearly on $\vec{H}$ that is

$$\vec{M} = \chi_m \vec{H} \tag{2.13}$$

where χ_m is the magnetic susceptibility of the medium. Substituting equation 2.13 into equation 2.12 leads to

$$\vec{B} = \mu_0(1 + \chi_m)\vec{H} = \mu\vec{H} \tag{2.14}$$

8

or

$$\vec{B} = \mu_0 \mu_r \vec{H} \tag{2.15}$$

where

$$\mu_r = 1 + \chi_m = \frac{\mu}{\mu_0}. \tag{2.16}$$

The constant μ is called the permeability of the material having unites of henrys/meter. The dimensionless quantity μ_r is the ratio of the permeability of a given material to that of free space and is known as the relative permeability of the material.

2.4   The Low Frequency Focus Beam System

In order to further reveal the problem of band edge corruption, a brief description of the system to be evaluated is needed. The system under evaluation is known as the Low Frequency Focus Beam (LFFB) System. In the context of material characterization, this particular system was designed to emulate plane-wave measurements of the transmission and reflection coefficients from planar samples where the solutions for intrinsic properties can be easily derived [5, 6, 19].

The LFFB system consists of horn antennas, collimating/focusing lenses and a sample holder, as depicted in Figure 2.4. The planar sheet to be measured is placed in the focused beam, typically at the beam waist of focus. This minimizes scattering do to the illumination of material edges, which is a well known inherent source of error for this particular type of system. The beam waist for this system varies as a function of frequency. Note, the reflection and transmission coefficients, which are vital for extracting ϵ and μ, are measured using a network analyzer.

2.5   Types of Calibration Techniques

The data that is recorded by the vector network analyzer is collected at the internally-housed detector elements. In order to acquire the sample/material scattering parameters, this data must be calibrated in order to account for the inherent systematic errors that are associated with the instrumentation and test fixture. Many
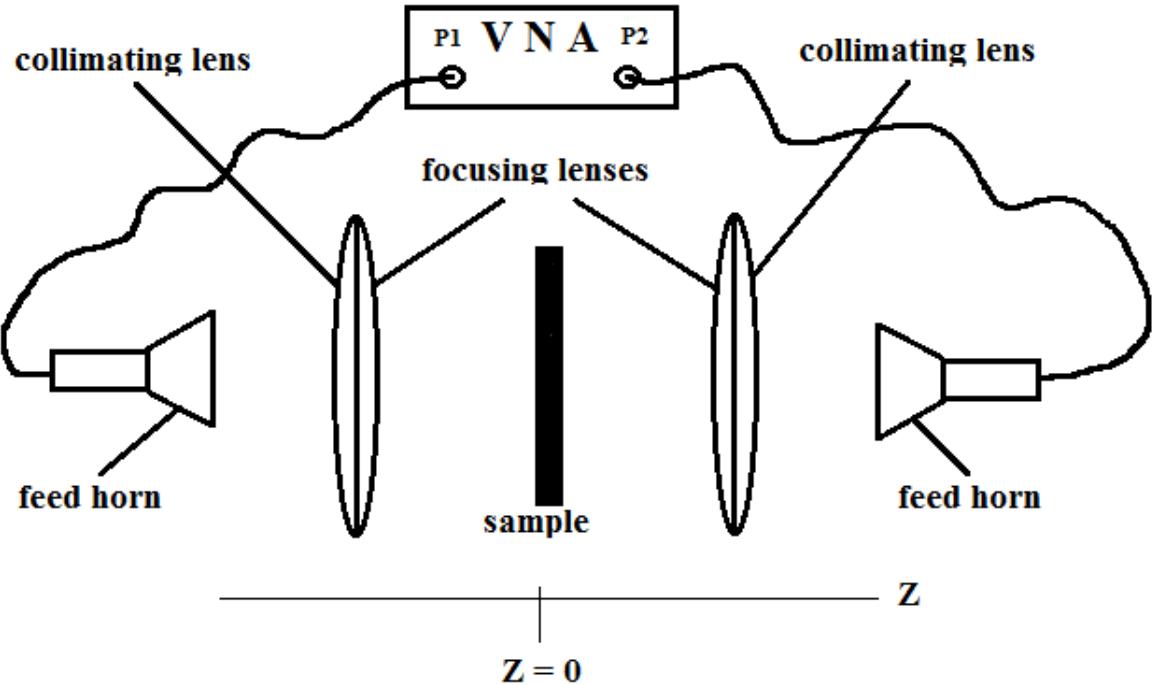
Figure 2.4:   The General Electric Low Frequency Focus Beam System

calibration techniques exist, each with their own obvious advantages and disadvantages. This section will focus on some of the more popular calibration techniques that have been used. The bulk of calibration processes can be separated into two groups. These groups are known as Standard Calibration and Self Calibration, as discussed next.

2.5.1 Standard Calibration.   The Standard Calibration is commonly known as the Short-Open-Load-Through (SOLT) technique. The downside to this calibration technique is that a large number of standards have to be measured, which can be time consuming. In addition, these standards may be difficult to achieve in practice. For example, when applying this calibration technique, as the frequency increases, the short and open standards are difficult to define because of the increasing effect of parasitic inductances and capacitances [3]. The SOLT calibration method is also rarely used for Free Space measurements because the Open standard is difficult to

10

fabricate, although attempts have been made using artificially-created periodic structure technology. Thus, for free-space or focus-beam systems, alternative calibration techniques are required, as described next.

2.5.2   Self Calibration.   Most other calibration methods fall into the category of Self Calibration techniques. These types of calibration techniques are different from Standard Calibration techniques because they use data obtained from transmission lines rather than data gained from discrete standards [10]. Self Calibration techniques can be broken down into two categories, Through-Reflect-Line (TRL) calibration and Through-Reflect-Match (TRM) calibration.

The TRL calibration technique utilizes a transmission Line of known length and impedance as one standard. This Line standard has to be significantly longer in electrical length than the Through line. For radio frequency applications, the length of transmission lines needed to encompass low frequencies become impractical [22]. TRL calibration also involves the use of a high-reflection standard which must be electrically the same for both test ports. Although this type of calibration technique when applied to the free space measurement system can result in error due to movement of actual components in the system, this method has been applied successfully in various experiments [6, 15–17]. Gagnon presents a study on the Misalignments in Quasi-Optical Measurements [4]. In reviewing this, it is concluded that a calibration technique that does not involve translation of the feed horns or movement of the sample lens is strongly advised. Slight misalignments cause error to manifest itself within the results that are hard to correct. Previous experiments suggest movement of the feed horn in order to realize the "Line" standard. A calibration technique that does not involve movement of the feed horns is sought after for the purposes of minimizing systematic errors. If the line standard is to be used, the difference between the two lengths of line must be approximately a quarter of wavelength at midband frequency, therefore the TRL is bandwidth limited [10]. In many cases of Free Space Measurement Systems, the horns are mounted to ensure their precise positioning in relation

to the collimating lenses. Thus, movement of the horns in order to record data for a "line" standard is not recommended.

The need for a better approach in calibrating this system led to alternative calibration methods. The Through-Reflect-Match (TRM) Calibration with the addition of some correction terms described in [5] is another validated calibration process. This process is fairly similar to the previously discussed TRL calibration method. Instead of using two transmission line standards, the TRM calibration utilizes only one transmission line based standard. A highly reflective standard is still needed. The major notable difference is brought about by the use of a Match standard instead of an additional transmission line measurement. The use of a Match standard is favorable by some scientists and engineers as it allows for fixed location of the horns, therefore less error will be introduced into the results by improper positioning of the horns [4]. The match standard also is not bandwidth limited. At the frequencies used for the purposes of this thesis, a true match standard is hard to achieve as broadband absorbing standards are difficult to fabricate

2.6 Time Domain Gating Technique

The time-domain gating calibration scheme utilizes a Reflect setup to initialize the reference calibration plane, where the VNA records the S_{11}^{cal} response in the frequency domain. This uncalibrated measurement contains systematic error caused by the constructive and destructive interference from multiple scatterers present in the system (i.e. horns, lenses, etc). Applying a Fourier Transform of this response to take it into the time-domain reveals the relative locations of the multiple reflections. This exemplifies a physically-intuitive response where the dominant reflection is caused by the inserted short while the other reflections are caused by inherent imperfections in the system. Multiple reflections from the collimating lenses are a source of these reflections, as well as the lenses [7]. These system imperfections are easily identified based on the time separation between pulses (see Figure 4.1).

The unwanted scatterers can be easily removed by applying time-domain gating to the response. This effectively removes the undesired responses and leaves only the dominant scatter produced by the reflective standard. Transforming this gated response back into the frequency domain produces the desired S_{11}^{cal} response of any additional clutter. This time-domain gated short measurement can then be utilized in conjunction with the following $Thru$ setup to calibrate the Free Space Measurement System.

The $Thru$ utilizes the S_{21}^{cal} response of an empty measurement in the frequency domain. Again, the data is transformed into the time-domain, gated and transformed back into the frequency domain, producing the desired S_{21}^{cal} response that can then be used to calibrate the system [7].

The two calibration measurements, the $Reflect$ and $Thru$, can now be related to the testing sample measurements, via the relations

$$S_{11}^{ms} = E_{RT} S_{11}^{sam}, \qquad (2.17)$$

$$S_{21}^{ms} = E_{TT} S_{21}^{sam}. \qquad (2.18)$$

E_{RT} and ETT represent the forward reflection and transmission tracking error terms respectively, discussed in Chapter 3. The transition region scattering parameters can be computed from the calibration measurements. Since the gated short and empty measurements are related to the transition region scattering parameters via

$$S_{11}^{cal} = E_{RT} S_{11}^{sh} = E_{RT}(-1), \qquad (2.19)$$

$$S_{21}^{cal} = E_{TT} e^{-\gamma_0 l_s}, \qquad (2.20)$$

where

$$k_0 = \omega \sqrt{\epsilon_0 \mu_0}, \qquad (2.21)$$

$$\gamma_0 = j k_0. \qquad (2.22)$$

13

Where l_s is the sample width. Therefore, the de-embeded sample scattering parameters can be obtained through substitution of equations(2.19) and (2.20) into equations (2.17) and (2.18), leading to

$$S_{11}^{sam} = -\frac{S_{11}^{ms}}{S_{11}^{cal}}, \tag{2.23}$$

$$S_{21}^{sam} = \frac{S_{21}^{ms}}{S_{21}^{cal}e^{\gamma_0 l_s}}. \tag{2.24}$$

The permittivity and permeability can be subsequently determined using the standard NRW [20] technique or Newton-Raphson [12] root search algorithm.

VNAs that have the ability to do real time Fourier Transforms are expensive and some labs don't have the capability. The main reason for researching an alternate approach to the time-domain gating technique is the fact that you essentially have to deemphasize through weighting important band-edge data due to windowing. Furthermore, the windowing size itself directly affects the extracted data. Depending on window size, more data in the lower and higher frequencies may become corrupted due to a weighting factor that is applied on the band edges in order to reduce side lobes, in an effort to increase SNR. The aim of this thesis focuses on extracting low frequency data, making the time-domain gating method unacceptable. Before proceeding,to the proposed three short calibration technique in chapter 3, the necessary background in material extraction is discussed.

2.7   Windowing

In order to understand the need for a better way to calibrate the Low Frequency Focus Beam System, a brief discussion on windowing in the frequency domain will be presented. As depicted in Figure 2.5, the use of a rectangular window captures all of the frequency data of interest. However, the downside to this window is that it only allows for a -13dB drop in the first side lobe level. This small decrease in side lobe levels can cause for systematic or environmental noises to be an issue when trying to extract important data. Note, the main side lobe width is extremely narrow, which can be advantageous in regards to resolution. Also depicted, for comparison is the
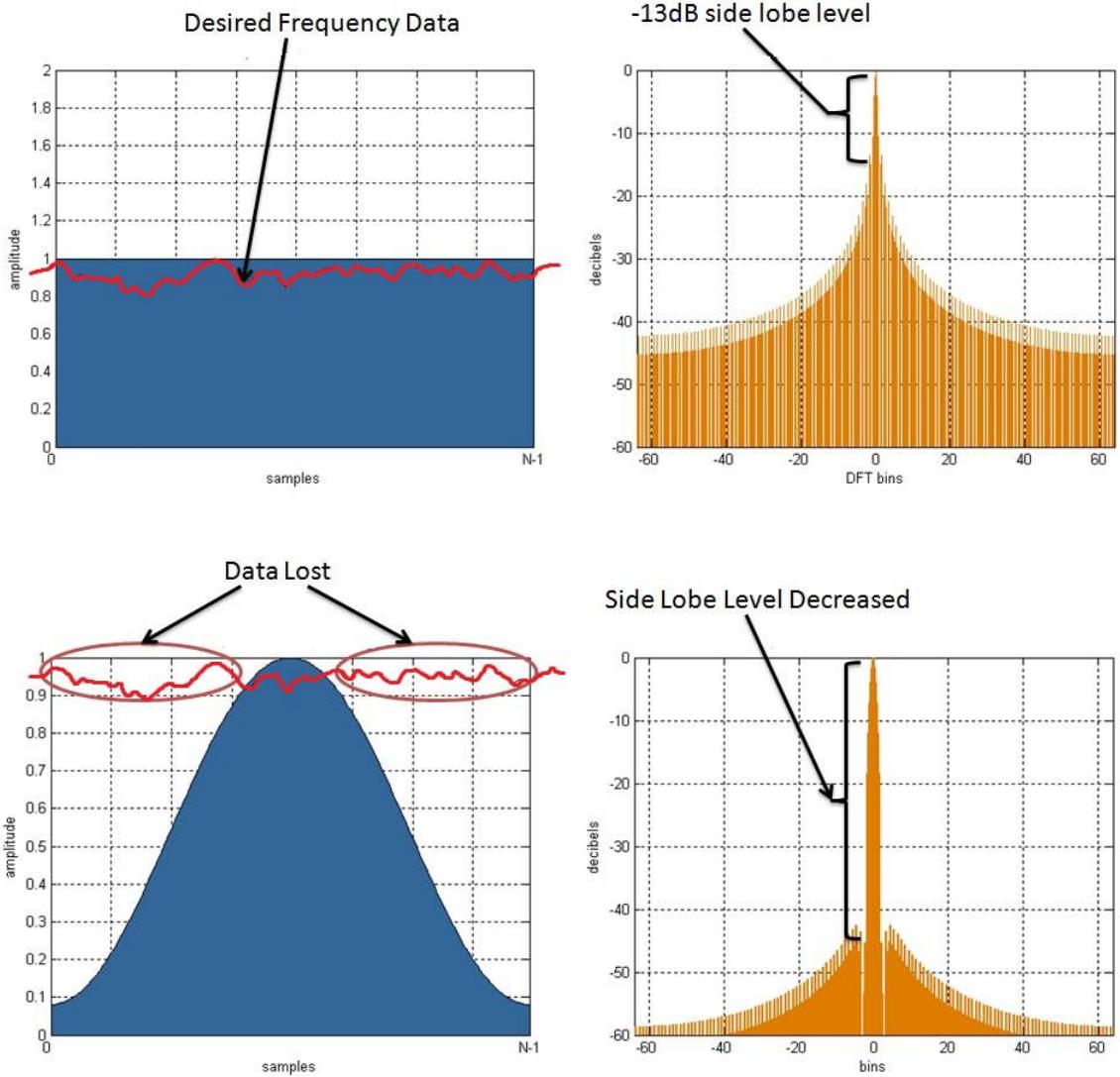
Figure 2.5:   The top picture represents the use of a rectangular window and its frequency response. The bottom picture represents the use of a hamming wind and its frequency response. This figure depicts the information that is lost due to a trade off when trying to decrease sidelobe levels.

use of a hamming window. It is evident that there is data in the high and low end of the bandwidths that is heavily weighted. Although the first side lobe is decreased dramatically, it comes at the expense of band edge data corruption. The three short calibration technique aims to eliminate the use of windowing all together in an effort to preserve the apparent data that is lost as depicted in Figure 2.5 as a result of windowing techniques.

2.8 Nicolson-Ross-Weir Technique

The Nicolson-Ross-Weir (NRW) technique allows for the extraction of the complex permittivity and permeability of a single layered material [20]. The algorithm itself requires two measured parameters: the transmission and reflection coefficients from the material under test. Thus, the forward (S_{11}, S_{21}) and reverse (S_{22}, S_{21}) scattering parameters can be utilized to compute the material parameters.

The formulation of the NRW technique compares the theoretical and experimentally measured S-parameters.

$$S_{11}^{thy}(\omega, \epsilon, \mu) - S_{11}^{exp}(\omega, \epsilon, \mu) = 0, \tag{2.25}$$

$$S_{21}^{thy}(\omega, \epsilon, \mu) - S_{22}^{thy}(\omega, \epsilon, \mu) = 0 \tag{2.26}$$

Where the theoretical S-Parameters can be formulated according to [6] as

$$S_{11}^{thy} = \frac{R(1 - P^2)}{1 - R^2 P^2} = S_{11}^{exp}, \tag{2.27}$$

$$S_{21}^{thy} = \frac{P(1 - R^2)}{1 - R^2 P^2} = S_{21}^{exp}. \tag{2.28}$$

A closed-form solution can be found by solving these nonlinear equations for R and P in terms of S_{11}^{exp} and S_{21}^{exp}. Solving these equations leads to the quadratic equation

$$R^2 - 2QR + 1 = 0 \tag{2.29}$$

$$Q = \frac{(S_{11}^{exp})^2 - (S_{21}^{exp})^2 + 1}{2S_{11}^{exp}} \tag{2.30}$$

which has the solution

$$R = Q \pm \sqrt{Q^2 - 1} \tag{2.31}$$

Since the magnitude of the interfacial reflection coefficient can never be greater than unity for a passive material, the proper root choice is simply the one which satisfies the requirement $|R| \leq 1$.

With the experimentally measured S-parameters related to R and P, the complex material parameters can now be determined. When utilizing a rectangular X-Band waveguide operating in the TE10 mode, assuming no gaps exist between the sample and perfectly conducting waveguide walls, the relative permittivity and permeability can be formulated as

$$R = \frac{z-1}{z+1}, z = \frac{Z}{Z_0} = \frac{j\omega\mu_0\mu_r/\gamma}{j\omega\mu_0/\gamma_0} = \mu_r\frac{\gamma_0}{\gamma} \tag{2.32}$$

In a free space measurement system, $k_c = 0$, thus

$$\gamma^2 = k_c^2 - k^2, \ k^2 = \omega^2\epsilon\mu, \ k_c^2 = 0 \tag{2.33}$$

$$P = e^{-\gamma l}, \gamma = -\frac{lnP}{l} = \sqrt{k_c^2 - k_0^2\epsilon_r\mu_r} \tag{2.34}$$

Therefore, ϵ_r and μ_r can easily be extracted using the following two equations.

$$\mu_r = z\frac{\gamma}{\gamma_0} = -\frac{lnP}{\gamma_0 l}(\frac{1+R}{1-R}) \tag{2.35}$$

$$\epsilon_r = \frac{k_c^2 - \gamma^2}{\mu_r k_0^2} = -\frac{k_c^2 - (lnP/l)^2}{k_0^2}\frac{lnP}{\gamma_0 l}(\frac{1+R}{1-R}). \tag{2.36}$$

2.9 Newton Raphson Method

This section focuses on a numerical technique that will be utilized to extract the complex permittivity (or permeability) of the device under test. Many numerical methods exist to determine the roots of a nonlinear equation. The Newton-Raphson method is a derivative-based root finding technique that only requires an initial guess of the root [12]. Convergence is not guaranteed, but if the method does converge, it does so much faster than in similar numerical bracketing methods, such as the bisection method [13].

The Newton-Raphson method is based on the principle that if the initial guess of the root of $f(x) = 0$ is at x_i, then by drawing a tangent line to the curve at

17

$f(x_i)$, the point x_{i+1} where the tangent crosses the x-axis is an improved estimate of the root. The method can be derived by using the Taylor expansion of an arbitrary nonlinear function $f(x)$

$$f(x + \Delta x) \cong f(x) + f'(x)\Delta x = 0 \tag{2.37}$$

Solving for Δx leads to

$$\Delta x = -\frac{f(x)}{f'(x)}, \tag{2.38}$$

which can then be expanded as

$$\Delta x = x_{i+1} - x_i = \Delta x = -\frac{f(x_i)}{f'(x_i)}. \tag{2.39}$$

This can then be rearranged to produce the following

$$x_{i+1} = x_i - \frac{f(x_i)}{f'(x_i)}. \tag{2.40}$$

The preceding equation is known as the Newton-Raphson formula for finding the roots (i.e., zeros) of nonlinear functions.

The Newton-Raphson Method can be modified to find the dielectric constant of a non-magnetic material. This is accomplished by setting the nonlinear function to either

$$f(x) = \begin{cases} |S_{11}^{thy}(\omega, \varepsilon) - S_{11}^{\exp}(\omega)| < tol, \ or \\ |S_{21}^{thy}(\omega, \varepsilon) - S_{21}^{\exp}(\omega)| < tol \end{cases} \tag{2.41}$$

where *tol* is a user defined tolerance (typically 1×10^{-7}). If the derivative cannot be found analytically, the numerical derivative of $f(x)$ can be approximately computed as

$$f'(x) = \lim_{\Delta x \to 0} \frac{f(x + \Delta x) - f(x)}{\Delta x} \approx \frac{f(x + \Delta x) - f(x)}{\Delta x} \tag{2.42}$$

The theoretical scattering parameters can be found through the use of wave transmission matrices, or A-parameters which describe the relationship at particular

18
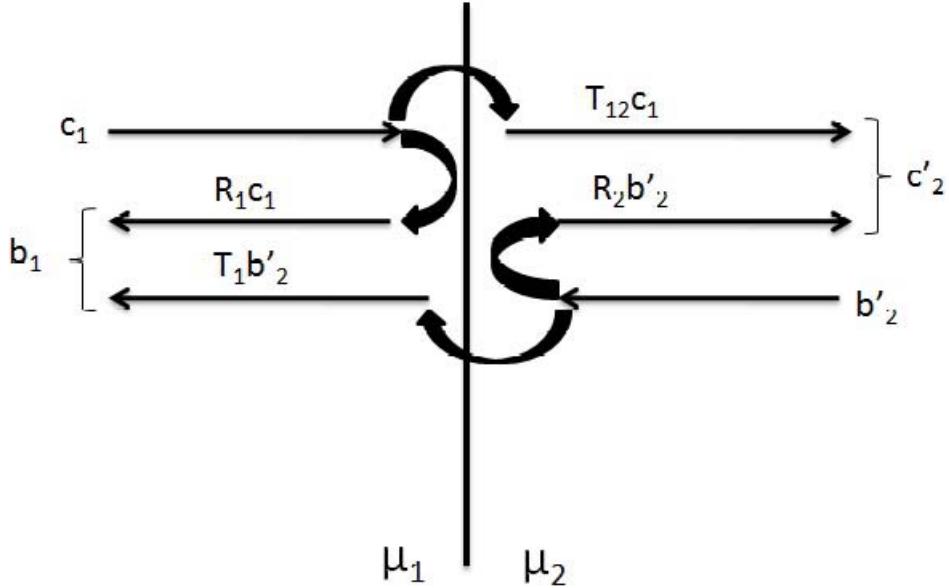
Figure 2.6:   Reflected and transmitted waves at a planar interface

reference planes between incident and reflected wave amplitudes. The general A-parameter formulation considers incident waves c_1 and b_2' on an interface from the left and right, respectively, as depicted in Figure 2.6. The respective interfacial reflection and transmission coefficient experienced by waves c_1 and b_2' are represented as R_1, T_{12} and R_2, T_{21} such that

$$c_2' = T_{21}c_1 + R_2b_2' \tag{2.43}$$

$$b_1 = R_1c_1 + T_{21}b_2', \tag{2.44}$$

which can be manipulated such that

$$c_1 = \frac{1}{T_{12}}c_2' - \frac{R_2}{T_{12}}b_2' \tag{2.45}$$

$$b_1 = \frac{R_1}{T_{12}}c_2' + \frac{T_{12}T_{21} - R_1R_2}{T_{12}}b_2'. \tag{2.46}$$

These equations lead to the following matrix expression

$$\begin{pmatrix} c_1 \\ b_1 \end{pmatrix} = \frac{1}{T_{12}} \begin{pmatrix} 1 & R_1 \\ R_1 & 1 \end{pmatrix} \begin{pmatrix} c'_2 \\ b'_2 \end{pmatrix} \tag{2.47}$$

This relationship describes the forward and reverse traveling waves immediately to the left and right of the interface. With the region assumed to be linear, homogeneous and isotropic, the waves c'_2 and b'_2 can be simply related to the corresponding waves c_2 and b_2 located a distance l from the interface as

$$c_2 = c'_2 e^{-\gamma l} \tag{2.48}$$

$$b'_2 = b_2 e^{-\gamma l} \tag{2.49}$$

This relationship can further be represented in matrix form as

$$\begin{pmatrix} c'_2 \\ b'_2 \end{pmatrix} = \begin{pmatrix} e^{\gamma l} & 0 \\ 0 & e^{\gamma - l} \end{pmatrix} \begin{pmatrix} c_2 \\ b_2 \end{pmatrix} \tag{2.50}$$

The A-parameter relationship between waves c_1, b_1 and c_2, b_2 is as follows

$$\begin{pmatrix} c_1 \\ b_1 \end{pmatrix} = \frac{1}{T_{12}} \begin{pmatrix} e^{\gamma l} & R_1 e^{-\gamma l} \\ R_1 e^{\gamma l} & e^{-\gamma l} \end{pmatrix} \begin{pmatrix} c_2 \\ b_2 \end{pmatrix} = \begin{pmatrix} A_{11} & A_{12} \\ A_{21} & A_{22} \end{pmatrix} \begin{pmatrix} c_2 \\ b_2 \end{pmatrix} \tag{2.51}$$

Thus, the generalized A-parameter wave matrix can be represented as

$$\begin{pmatrix} A_{11} & A_{12} \\ A_{21} & A_{22} \end{pmatrix} = \frac{1}{1+R} \begin{pmatrix} e^{\gamma l} & \mathrm{Re}^{-\gamma l} \\ \mathrm{Re}^{\gamma l} & e^{-\gamma l} \end{pmatrix} \frac{1}{1-R} \begin{pmatrix} 1 & -R \\ -R & 1 \end{pmatrix} \tag{2.52}$$

20

This equation may be simplified by letting $P = e^{-\gamma l}$ and applying matrix multiplication to produce

$$
\begin{pmatrix} A_{11} & A_{12} \\ A_{21} & A_{22} \end{pmatrix} = \frac{1}{P(1-R^2)} \begin{pmatrix} 1 - R^2 P^2 & -R(1-P^2) \\ R(1-P^2) & P^2 - R^2 \end{pmatrix} \tag{2.53}
$$

The Scattering parameters can be determined from the well known relations

$$
\begin{pmatrix} S_{11} & S_{12} \\ S_{21} & S_{22} \end{pmatrix} = \frac{1}{A_{11}} \begin{pmatrix} A_{21} & A_{11}A_{22} - A_{21}A_{12} \\ 1 & -A_{12} \end{pmatrix} \tag{2.54}
$$

Through substitution, you obtain the scattering relations

$$
S_{11} = S_{22} = \frac{R(1-P^2)}{1 - R^2 P^2} \tag{2.55}
$$

$$
S_{21} = S_{12} = \frac{P(1-R^2)}{1 - R^2 P^2} \tag{2.56}
$$

With an analytic formulation of the theoretical scattering parameters developed, the general process of the Newton-Raphson method can then be invoked to determine the complex roots of the nonlinear function, which in this case produces the relative permittivity of the measured sample. Note, if the sample is also magnetic, a two-dimensional root search can be used to extract both ϵ and μ. In this case, S_{11} and S_{21} are required.

2.10   Numerical Position Independent Method

Simple techniques exist to de-embed the sample position planes from the calibrated reference planes, though this requires exact knowledge of the sample position. Therefore, a formulation independent of the sample position would lead to greater precision of the extracted material parameters. This formulation can be accomplished using a computational algorithm, such as the Newton-Raphson method, to derive complex material parameters from the measured scattering parameters.

The position independent formulation effectively eliminates any uncertainties in the sample position. The Newton-Raphson method can be modified to position-independently find the complex parameters of a dielectric and magnetic material [8]. In this case the method must be adapted to solve for the complex roots of two nonlinear coupled equations, such as

$$f(x,y) = |S_{11}^{thy}(\omega, \epsilon, \mu) S_{22}^{thy}(\omega, \epsilon, \mu) - S_{11}^{exp} S_{22}^{exp}| < tol \tag{2.57}$$

$$g(x,y) = |S_{21}^{thy}(\omega, \epsilon, \mu) S_{12}^{thy}(\omega, \epsilon, \mu) - S_{21}^{exp} S_{12}^{exp}| < tol \tag{2.58}$$

With position uncertainty completely removed, the two functions $f(x,y)$ and $g(x,y)$ can be shown in Taylor expansion form

$$f(x + \Delta x, y + \Delta y) \cong f(x,y) + \frac{\delta f(x,y)}{\delta x} \Delta x + \frac{\delta f(x,y)}{\delta y} \Delta y \tag{2.59}$$

$$g(x + \Delta x, y + \Delta y) \cong g(x,y) + \frac{\delta g(x,y)}{\delta x} \Delta x + \frac{\delta g(x,y)}{\delta y} \Delta y. \tag{2.60}$$

This can be manipulated into matrix format as

$$\begin{pmatrix} f_x & f_y \\ g_x & g_y \end{pmatrix} \begin{pmatrix} \Delta x \\ \Delta y \end{pmatrix} = - \begin{pmatrix} f \\ g \end{pmatrix} \tag{2.61}$$

where the application of the inverse matrix will isolate the new guesses for the two coupled nonlinear equations as

$$\begin{pmatrix} x_{i+1} \\ y_{i+1} \end{pmatrix} = \begin{pmatrix} x_i \\ y_i \end{pmatrix} - \frac{1}{f_x g_y - f_y g_x} \begin{pmatrix} g_y & -f_y \\ -g_x & f_x \end{pmatrix} \begin{pmatrix} f \\ g \end{pmatrix} \tag{2.62}$$

The numerical partial derivative of $f(x)$ and $g(x)$ can be approximately computed as

$$f_x(x) = \lim_{\Delta x \to 0} \frac{f(x + \Delta x) - f(x)}{\Delta x} \approx \frac{f(x + \Delta x) - f(x)}{\Delta x} \tag{2.63}$$

$$g_x(x) = \lim_{\Delta x \to 0} \frac{g(x + \Delta x) - g(x)}{\Delta x} \approx \frac{g(x + \Delta x) - g(x)}{\Delta x} \qquad (2.64)$$

where the partial derivatives with respect to x can be computed in similar format. The general process of the Newton-Raphson method then follows where the subsequent iterations determine the complex roots of the nonlinear functions, which in this case produce the relative permittivity and permeability of the measured sample.

2.11 Summary

A discussion of permittivity and permeability was necessary as the extraction of these parameters are the main focus of this research. A brief description of the Low Frequency Focus Beam System was given as well as a break down of the components that allow this system to be a viable way of measuring material constitutive parameters. A review of calibration techniques that are in practice now at GE for the free space measurement system was provided. This research leads to the conclusion that there is not one overall superior calibration technique, they all have positives and negatives. Bandwidth limitations and calibration standard errors were two of the main limitations of most techniques. There is no way in practice to directly extract material constitutive parameters, so various material parameter extraction techniques were discussed. These various techniques should help in the analysis of the three short calibration technique as information gained from the reflective standards may prove to be critical. A discussion of the current time-gating based calibration technique used by General Electric was given in an effort to exemplify the need for an improved calibration technique.

III. Development of the Three Short Calibration Technique

In the previous chapter, it was shown that an alternative focused beam calibration technique may be beneficial for extracting meaningful uncorrupted data near band edges. In this chapter, a three-short calibration technique which does not rely on windowing or gating is proposed and developed for the focused beam system.

3.1 Universal 12-Term Error Model

An effective method to calibrate the Low Frequency Focus Beam System is explored here, namely, the three short calibration technique. The three short calibration technique involves making 3 initial measurements of highly reflective standards placed at different specified positions, along with the general "Thru" measurement in order to obtain sufficient data to be able to solve for all the error terms that are encompassed in the "12-term error model" [18]. The three short calibration procedure involves a 12-term error model (6-term model forward, 6-term model reverse). By solving for all the error terms, an accurate and robust measurement of the material properties can be performed. This section will focus on the development of the 12-term error model and the three short calibration technique used to solve it.

The three short calibration technique has been successfully applied to network analyzers that have been used in conjunction with stripline systems in the past [9]. The motivation for developing theory to apply this calibration technique to the Low Frequency Focus Beam System was discussed previously.

The focus beam system that is available at the Air Force Institute of Technology is designed to record data in the ranges between 4-18Ghz. The focus beam system used for the experimentation in this thesis available at GE allows for measurements to be taken in the ranges between 0.5 and 6GHz, with interest in the UHF and L band frequency range [14]. With proper calibration, this allows the engineer to accurately predict how a material will interact when illuminated by an electromagnetic wave produced by a VHF or UHF radar. VHF and UHF radars are generally used for very long-range surveillance, because of the ability to obtain very large power-
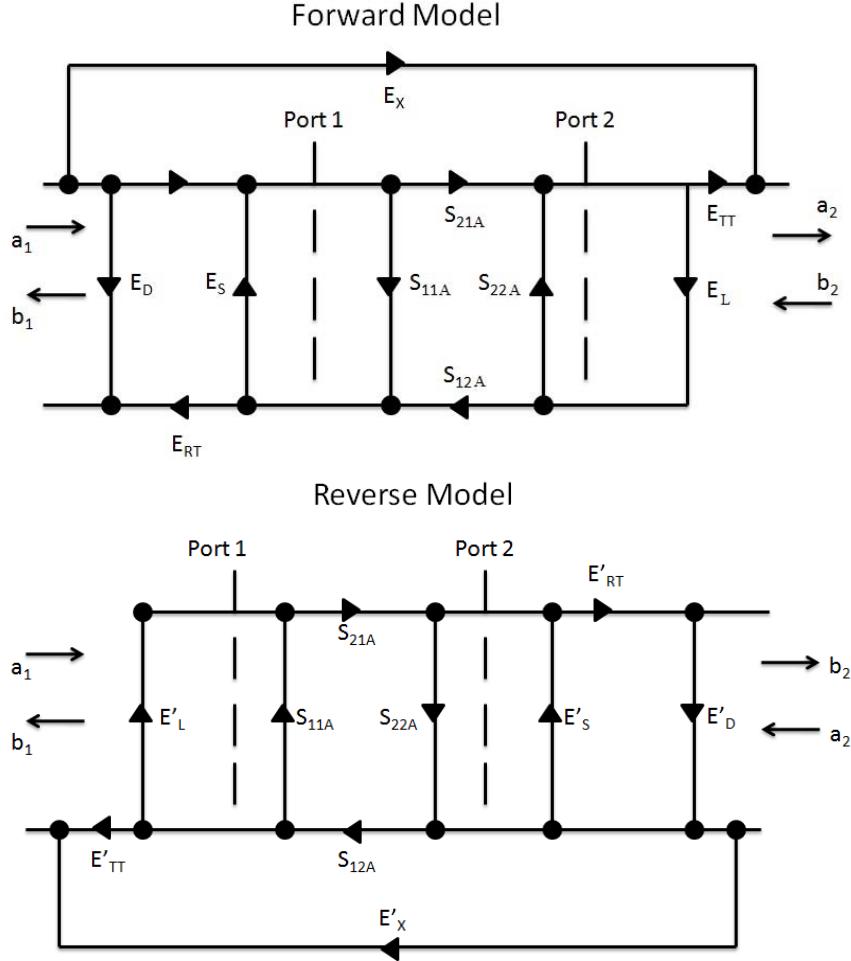
Figure 3.1: This figure represents the forward and reverse signal flow diagram of the twelve term error model.

aperture products at the lower frequencies and their favorable clutter and propagation characteristics [14]. With the presence of these threats, it is important to know how a material will react in the presence of that field in those low frequencies.

The relationship between the measured S-parameters at the NWA detector and the sample-plane S-parameters defined by the setup of the system is the foundation of the 12-term error model. A signal flow diagram is presented in Figure 3.1 in order to represent the error terms of the twelve term error model which are defined as follows

- E_D = forward directivity
- E_S = forward source match

- E_{RT} = forward reflection tracking

- E_L = forward load match

- E_{TT} = forward transmission tracking

- E_X = forward isolation

- E'_D = reverse directivity

- E'_S = reverse source match

- E'_{RT} = reverse reflection tracking

- E'_L = reverse load match

- E'_{TT} = reverse transmission tracking

- E'_X = reverse isolation

The equations to derive the actual sample S-Parameters at the reference planes (S_{11A}, S_{12A}, S_{21A}, and S_{22A}) as depicted in Figure 3.1 from the measured detector S-parameters (S_{11ms}, S_{12ms}, S_{21ms}, and S_{22ms}) described by [22] and depicted in Figure 3.2 are listed below. Notice that each actual S-parameter is a function of all four measured S-parameters. The network analyzer must make a forward and reverse sweep to update any one S-parameter.

$$S_{11A} = \frac{\left(\frac{S_{11ms}-E_d}{E_{RT}}\right)\left(1+\frac{S_{22ms}-E'_D}{E'_{RT}}E'_S\right) - E_L\left(\frac{S_{21ms}-E_x}{E_{TT}}\right)\left(\frac{S_{12ms}-E'_X}{E'_{TT}}\right)}{\left(1+\frac{S_{11ms}-E_d}{E_{RT}}E_S\right)\left(1+\frac{S_{22ms}-E'_D}{E'_{RT}}E'_S\right) - E'_L E_L\left(\frac{S_{21ms}-E_x}{E_{TT}}\right)\left(\frac{S_{12ms}-E'_X}{E'_{TT}}\right)}$$

$$(3.1)$$

$$S_{21A} = \frac{\left(\frac{S_{21ms}-E_x}{E_{TT}}\right)\left(1+\frac{S_{22ms}-E'_D}{E'_{RT}}\right)(E'_S - E_L)}{\left(1+\frac{S_{11ms}-E_D}{E_{RT}}E_S\right)\left(1+\frac{S_{22m}-E'_D}{E'_{RT}}E'_S\right) - E'_L E_L\left(\frac{S_{21ms}-E_X}{E_{TT}}\right)\left(\frac{S_{12ms}-E'_X}{E'_{TT}}\right)}$$

$$(3.2)$$

26

$$S_{12A} = \frac{\left(\frac{S_{12ms}-E'_x}{E'_{TT}}\right)\left(1+\frac{S_{11ms}-E_D}{E_{RT}}\right)(E_S-E'_L)}{\left(1+\frac{S_{11ms}-E_D}{E_{RT}}E_S\right)\left(1+\frac{S_{22ms}-E'_D}{E'_{RT}}E'_S\right)-E'_LE_L\left(\frac{S_{21ms}-E_X}{E_{TT}}\right)\left(\frac{S_{12ms}-E'_X}{E'_{TT}}\right)}$$
$$(3.3)$$

$$S_{22A} = \frac{\left(\frac{S_{22ms}-E'_d}{E_{RT}}\right)\left(1+\frac{S_{11ms}-E_D}{E'_{RT}}E'_S\right)-E_L\left(\frac{S_{21ms}-E_x}{E_{TT}}\right)\left(\frac{S_{12ms}-E'_X}{E'_{TT}}\right)}{\left(1+\frac{S_{11ms}-E_d}{E_{RT}}E_S\right)\left(1+\frac{S_{22ms}-E'_D}{E'_{RT}}E'_S\right)-E'_LE_L\left(\frac{S_{21ms}-E_x}{E_{TT}}\right)\left(\frac{S_{12ms}-E'_X}{E'_{TT}}\right)}$$
$$(3.4)$$

Solving for the unknown error terms requires twelve measurements [9]. Each measurement represents a separate, unique equation; thus, 12 equations are required to solve for 12 unknowns. Two equations come from measuring a matched load on each cable leading to the DUT:

$$S_{21}^{ml} = 0, \text{ and} \tag{3.5}$$

$$S_{12}^{ml'} = 0. \tag{3.6}$$

Four equations come from an empty focus beam system measurement:

$$S_{11}^{e} = 0, \tag{3.7}$$

$$S_{21}^{e} = 1, \tag{3.8}$$

$$S_{22}^{e'} = 0, \text{ and} \tag{3.9}$$

$$S_{12}^{e'} = 1. \tag{3.10}$$

The remaining six equations are from inserting a short in the sample holder. By varying the placement of the short, six unique equations (i.e., cal standard definitions) can be formed:

$$S_{11}^{sh1} = -e^{-j2k_0(-d)}, \tag{3.11}$$
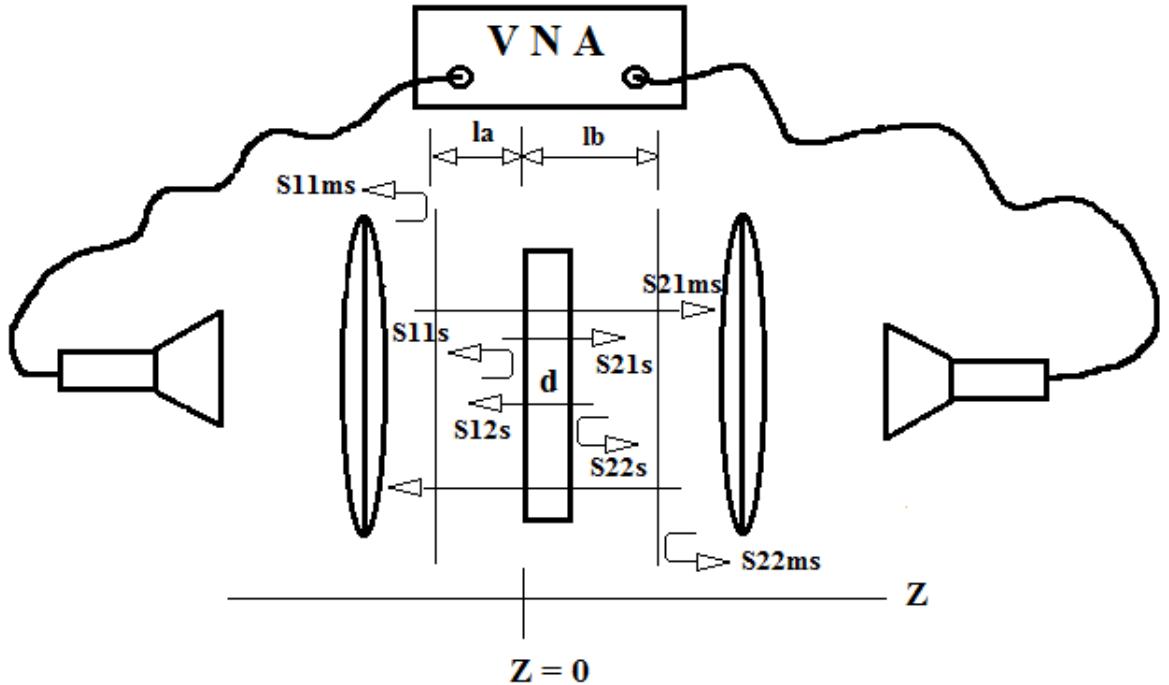
Figure 3.2: A depiction of the phase shift caused by the sample width

$$S_{22}^{sh1'} = -e^{-j2k_0(d-w)},\qquad(3.12)$$

$$S_{11}^{sh2} = -1,\qquad(3.13)$$

$$S_{22}^{sh2'} = -e^{-j2k_0(-w)},\qquad(3.14)$$

$$S_{11}^{sh3} = -e^{-j2k_0 d}, \text{ and}\qquad(3.15)$$

$$S_{22}^{sh3'} = -e^{-j2k_0(-[d+w])}.\qquad(3.16)$$

After the calibration is performed, post processing still has to be implemented to take into account the phase shift caused by the sample width d. From Figure 3.2 the following actual sample S-Parameters are derived.

$$S_{11}^s = S_{11}^{meas} e^{j2k_0 l_a},$$

$$S_{21}^s = S_{21}^{meas} e^{j2k_0(l_a+l_b+-d)},$$

$$S_{22}^s = S_{22}^{meas} e^{j2k_0(l_b - d)}, \text{ and}$$

$$S_{12}^s = S_{12}^{meas} e^{j2k_0(l_b - l + l_a)}.$$

With the assumption that l_a and l_b are both equal to 0, meaning the calibration measurement reference plane now is positioned at $z = 0$, the following relations exist.

$$S_{11}^s = S_{11}^{ms} \tag{3.17}$$

$$S_{21}^s = S_{21}^{ms} e^{-jk_0 d} \tag{3.18}$$

$$S_{12}^s = S_{12}^{ms} e^{-jk_0 d} \tag{3.19}$$

$$S_{22}^s = S_{22}^{ms} e^{-j2k_0 d} \tag{3.20}$$

With the S-parameters of the actual sample written in terms of the measured S-parameters, the material properties can be calculated using one of the various analytical or numerical techniques.

3.2 Derivation of Short Placements

The previous section provided a review of the 12-term error model that describes the systematic errors that are inherent in network analyzers. The three short calibration technique allows for six of the twelve error terms to be corrected by unique placement and measurement of a highly reflective standard during the calibration process. This section will focus in detail on how these unique locations are derived.

The three short calibration technique is a band limited calibration technique. The reference planes that are used for direct placement of the highly reflective standards used to record phase changes are dependent upon the bandwidth that will be used in the experiment. When placing the shorts in the system, spacing is extremely important. The purpose of measuring a short in three different positions is to gain the six unique equations (three from forward measured and three from reverse measurements) required to solve the 12-term error function. If placed improperly, S_{11}^{sh1}
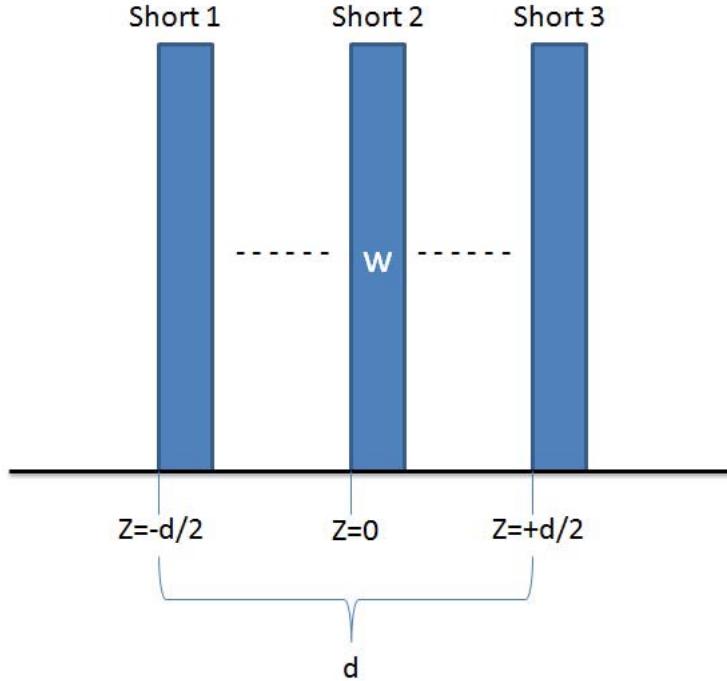
Figure 3.3: A depiction of the translation of the short standards

and S_{11}^{sh3} (defined by the Port 1 measured reflection coefficients of short 1 and short 3 respectively), for example, could be equal (i.e. degenerate). This would result in one fewer equations than unknowns. With short one placed at $-d/2$ and later short three placed at $d/2$ the distance between the two front faces is d as shown in Figure 3.3. If d is equal to $\frac{\lambda}{2}$ (λ being the wavelength), the effective phase delay seen at each short will be the same. In order to correct for this phase ambiguity, one may impose an 80% safety margin on that phase limit to ensure uniqueness. Thus, the goal is to keep the distance d to less than $\frac{2}{5}\lambda$.

The focus of this thesis is to be able to extract accurate and dependable low frequency material constitutive parameter data. As mentioned previously, the three short calibration technique is band limited so an initial determination of the bandwidth to be used in the experiment is of importance. A bandwidth of 500MHz to 2GHz is the chosen focus for all the experimentation. With an upper frequency established, derivation of appropriate spacing may be initiated.

The first step in this process is to calculate the $\frac{2}{5}\lambda$ distance for maximum short spacing. This derived distance will nullify the possibility of one short being a degenerate of another. The maximum frequency for this experiment is established to be 2GHz. By placing this frequency into the equation for wavelength, it is shown that

$$\lambda = \frac{c}{f} = 15cm \tag{3.21}$$

Dividing this wavelength by 2 and multiplying by the 80 percent safety factor establishes the maximum spacing distance d between the shorts which is shown to be

$$\frac{15cm}{2} \times 80\% = 6cm. \tag{3.22}$$

By specifying a maximum spacing distance of 6cm, instead of 7.5cm (without multiplication by the safety factor), one can theoretically evade the possibility of having a degenerate error.

3.3 Phase Angle of Multiple Shorts

There is another alternative viewpoint that can be implemented to ensure that the distance between the shorts will not introduce non-uniqueness into the results. This can be done by examining the phase term of each short and finding its location on the unit circle as depicted in Figure 3.4. Upon examining the equation defining S_{11}^{sh1}, one can easily deduce the phase term as

$$\Theta_{sh1} = 2k_0 d \tag{3.23}$$

where

$$k_0 = \frac{2\pi}{\lambda}. \tag{3.24}$$

In order to gain a visual perspective behind the phase term, 2π will be represented as 360°. The wavelength at 500MHz is 60cm long and the wavelength at 2GHz is 15cm. With all of these constants defined, a mathematical check of the difference in phase

from one translation to the next may be shown.

$$\Theta_{sh1} = 2k_0(3cm) = 2 \times \frac{2\pi}{\lambda}3cm = 2 \times \frac{360°}{15cm} \times 3cm = 144°$$

$$\Theta_{sh2} = 2k_0(0cm) = 2 \times \frac{2\pi}{\lambda} \times 0cm = 2 \times \frac{360°}{15cm} \times 0cm = 0°$$

$$\Theta_{sh3} = 2k_0(-3cm) = 2 \times \frac{2\pi}{\lambda}d = 2 \times \frac{360°}{15cm} \times (-3cm) = -144°$$

The phases $144°$, $0°$, and $-144°$ are very well spaced around the unit circle. This gives confidence that at 2GHz, the phases of the uniquely placed shorts will not introduce error into the results due to possible degeneracy. With the upper limit theoretically tested, the same process must now be completed for the lower limit of 500MHz to ensure sufficient uniqueness of the short standards. Analyzing the multiple shorts at 500MHz produces the results

$$\Theta_{sh1} = 2k_0(3cm) = 2 \times \frac{2\pi}{\lambda}d = 2 \times \frac{360°}{60cm} \times 3cm = 36°$$

$$\Theta_{sh2} = 2k_0(0cm) = 2 \times \frac{2\pi}{\lambda}d = 2 \times \frac{360°}{60cm} \times 3cm = 0°$$

$$\Theta_{sh3} = 2k_0(-3cm) = 2 \times \frac{2\pi}{\lambda}d = 2 \times \frac{360°}{60cm} \times (-3c)m = -36°$$

Although the difference between phases decreased with decreasing frequency, the obtained phase angle difference of $36°$ is sufficiently resolved by the NWA to ensure uniqueness.

3.4   Time Delays

In order to properly calibrated the VNA, the exact placement of the shorts have to be recorded in terms of the time delays with respect to the $z = 0$ reference plane, with $z = 0$ being the position where the sample will be placed. In addition the Empty/Thru time offset will be set to 0.
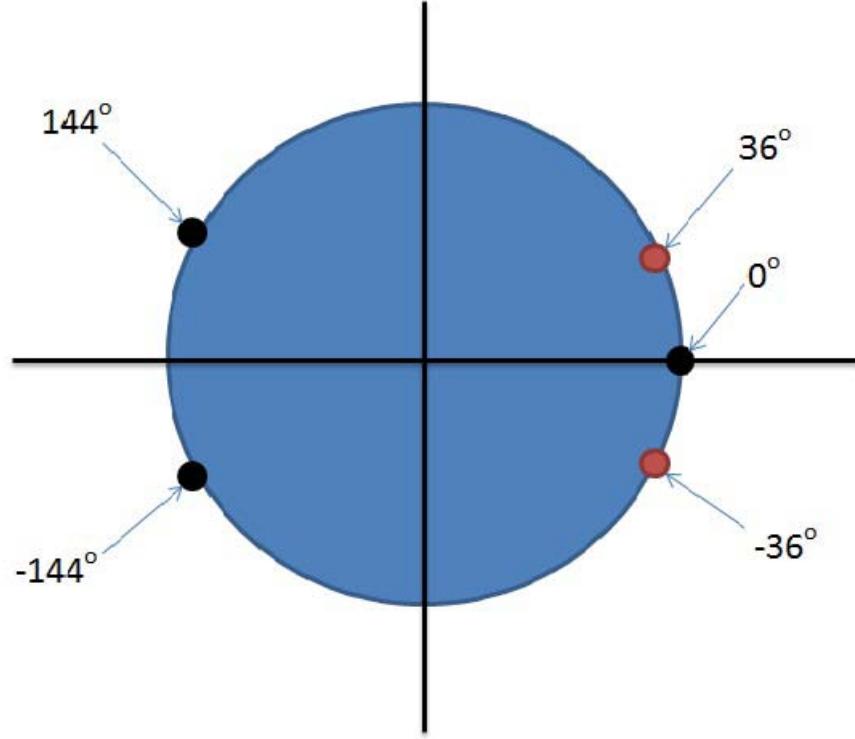
Figure 3.4: This figure represents the phase angles derived from the placement of the multiple shorts. The black marks represent the phase angles obtained at the high end of the bandwidth (2GHz) and the red marks represent the phase angles obtained by the low end of the bandwidth (500MHz)

In referencing the multiple shorts by measurements made from Port 1 (forward direction), the time constant offsets are defined as

$$t^f_{sh1} = \frac{-d}{c}, \tag{3.25}$$

$$t^f_{sh2} = \frac{0}{c}, \text{and} \tag{3.26}$$

$$t^f_{sh3} = \frac{d}{c} \tag{3.27}$$

where d is the offset distance from the $z = 0$ reference plane (3cm) and the speed of light, c, is a constant measured at 299,792,458 meters per second.

Table 3.1: This table represents the time delays that were derived and input as constants into the network analyzer. The subscripts f and r representing forward and reverse direction respectively.

Short	Time Delay (ps)
$Sh1_f$	-100.0692
$Sh1_r$	89.47857
$Sh2_f$	0
$Sh2_r$	-10.59066
$Sh3_f$	100.0692
$Sh3_r$	-110.65989

In referencing the multiple shorts by measurements made from Port 2 (reverse direction), the time constant offsets are defined as

$$t_{sh1}^r = \frac{d - w}{c},$$

(3.28)

$$t_{sh2}^r = \frac{-w}{c}, \text{and}$$

(3.29)

$$t_{sh3}^r = \frac{-(d + w)}{c}$$

(3.30)

where w is the width of the reflective standard. This width must be taken into account in order for accurate time constants to be defined.

Table 3.1 displays the derived time constants that will be input into the network analyzer. Definition of these time constants solves for six of the 12 equations in the universal 12 term error model. As previously discussed, four more equations will come from an empty/thru measurement where t_{delay} will be set to 0. The last two equations come from the *Isolation* measurement, which is used to calibrate out the cross talk terms associated with the 12 term error model. With all these measurements in place, the NWA is now ready for material measurements.

3.5   Imprecise Translations

A cause of error in the results obtained is may be attributed to improper positioning of the short reference planes. In order for this technique to be effective,

34

precise placement of the shorts is needed. The translation mechanism used for the LFFB is shown in Figure 3.5. This mechanism appears to be accurate down to .001 inches. The reference plane is translated by rotating this crank until the new position is reached. There is not only the obvious chance of mechanical error associated with this mechanism, but also the added chance of human error in operating the mechanism. Although care was taken in all measurements, there was not a way to truly validate precise translation. Figure 3.5 shows how the 3-Short Positions were marked on the test bench. These positions were not only attempted to be reached by the translation mechanism, but also they were measured with a ruler and marked as depicted. The ruler measurements and the translation mechanism did not agree in all translations, but accuracy was assumed to be within $\pm$ .005 inch. Short 1 was measured at the mark farthest to the left, followed by Short 2 in the middle ($z = 0$), and Short 3 farthest to the right. Once all 3 Shorts were measured, the sample holder was returned to the position of Short 2 at $z = 0$ and sample measurements were taken. One can easily see that without a very precise way to define the reference planes, the multiple translations can easily cause unwanted phase errors, and in turn add error to the results. In future works, this can be quantitatively validated by performing an uncertainty analysis. It is noted that a precision laser alignment system be implemented in future works.

3.6   Summary

The well known error terms that are associated with network analyzers were reviewed and discussed. Characterization of these error terms are sought after by the use of calibration procedures. The three short calibration technique allows twelve measurements to be performed in order to solve for the twelve unknown error terms. Since the three short calibration technique is band limited, a derivation of the maximum spacing constraint was established and a distance of $\pm 3cm$ from the $z = 0$ reference plane was computed for the short placements. This distance includes a 20% safety factor that ensures non-degeneracy. The phase angles produced by the place-

35

ment of the shorts was investigated. The maximum frequency of the bandwidth (i.e. 2 GHz) produced a phase angle difference of $\pm 144°$, between shorts and a phase angle difference of $\pm 36°$, at 500MHz, which is well within the phase accuracy of the NWA. The appropriate time constants were input into the NWA calibration kit definition and a discussion of phase advances and phase delays was provided. In the next chapter, the extracted results of two dielectric materials will be presented based on the time-domain and the proposed three-short calibration technique outlined above.
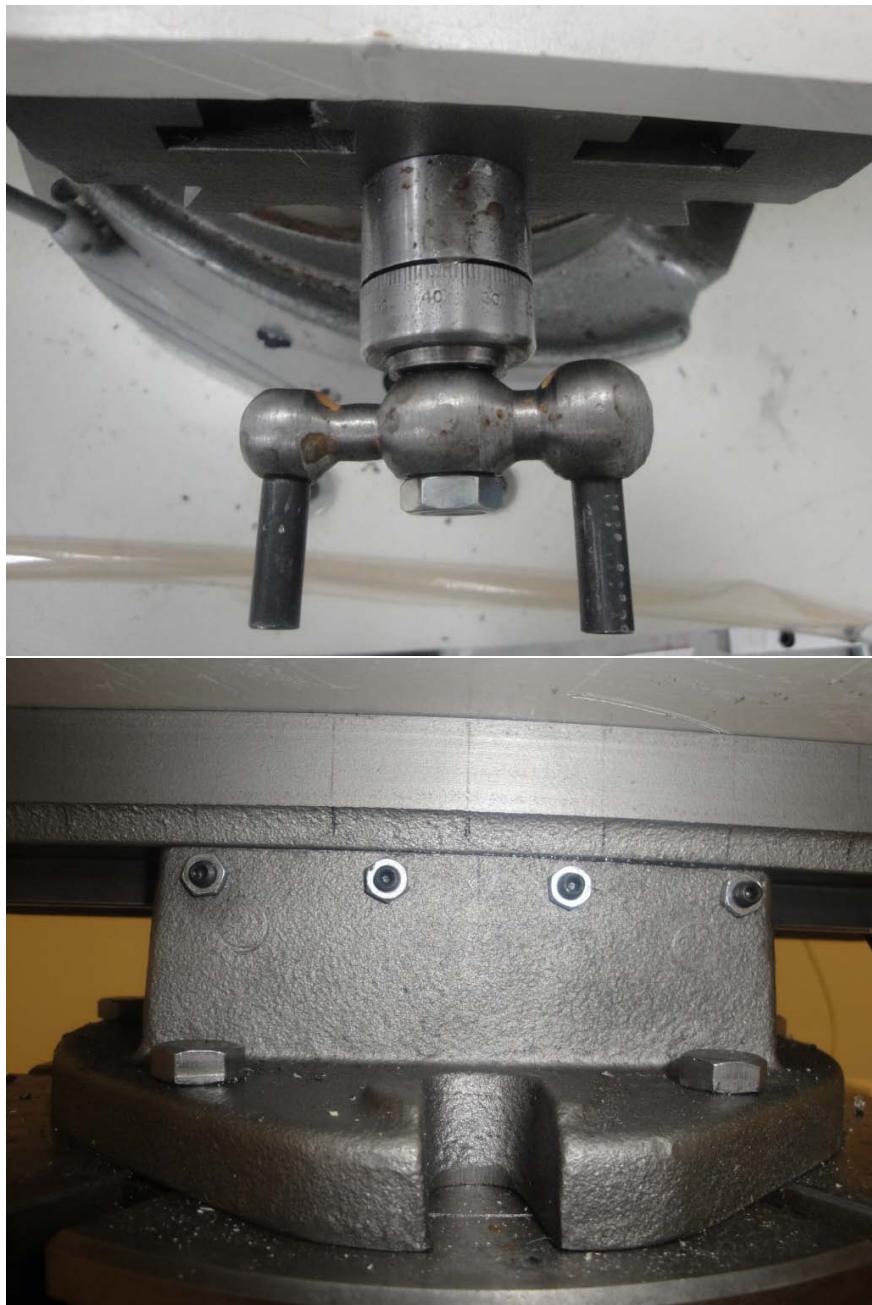
Figure 3.5:   Translation Mechanism

IV. Results

In this chapter, the permittivity of two dielectric samples will be extracted based on the time domain and the proposed three short calibration technique. All measurements were performed using the Low-Frequency Focus Beam System in the frequency regime of 0.5-2GHz. Table 4.1 presents the test matrix used for experimentation in this thesis. In each measurement, all four scattering parameters were recorded. It should be noted that a time domain uncalibrated metal plate response was recorded to give physical insight to the system imperfections. This was proceeded by the calibration standards,three shorts and a $THRU$ measurement, with their results being used to solve the 12-term error model. Lastly, calibrated measurements were taken of the two known dielectrics. It should be noted that the *isolation* measurements were omitted under the assumption that cross talk was negligible.

Table 4.1:   This table presents the test matrix that will is used during experimentation. The position $z = 0$ refers to the desired reference plane where actual sample measurements will be taken.

Sample Holder Position	Object	Width(inches)
$z = 0$ (uncalibrated)	metal plate	0.125
BEGIN CALIBRATION		
3cm toward Port A (SHORT 1)	metal plate	0.125
$z = 0$ (SHORT 2)	metal plate	0.125
3cm toward Port B (SHORT 3)	metal plate	0.125
$z = 0$ (THRU)	empty	0
APPLY CALIBRATION		
$z = 0$	empty	0
$z = 0$	fiberglass	0.183
$z = 0$	plexiglas	0.185

4.1   Time Domain Response of Metal Plate

In order to do a complete analysis of the Three Short Calibration Technique as applied to the LFFB system, multiple measurements were taken. The first measurement that will be examined is the time domain uncalibrated response of the metal plate used as the reflective standard during the calibration process. Viewing this data in the time domain allows for the engineer to physically see the obstructions in
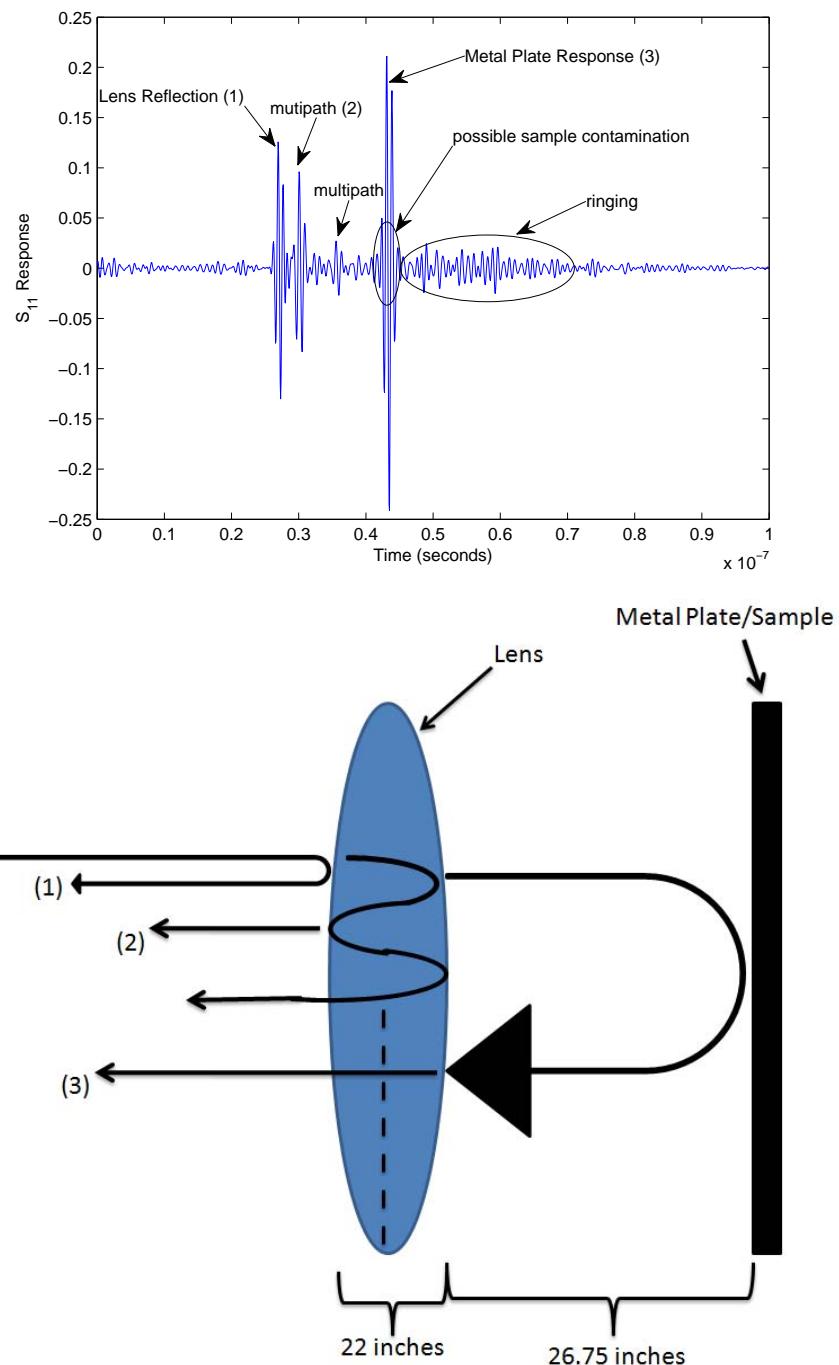
Figure 4.1: Time domain response of metal plate at sample measurement plane.

the system that may cause interference, which would lead to ripples in the extracted constitutive parameter data.

In viewing Figure 4.1, one can easily note the main responses of the system. At around 27 nanoseconds, the first response occurs. It is well known that electromagnetic waves travel at approximately 1 foot per nanosecond in free space. We must also note that this is two way time travel, so a response at 27 nanoseconds, is indicative of a reflection at approximately 13.5 nanoseconds one way travel, or 13.5 feet from the NWA. It must be noted that this is only an approximate location due to the fact that electromagnetic waves travel at a different speed when in coaxial cables, antennas, and dielectric lenses. Included in this length of travel are cables leading to the feed horn, distance through the horn, and the free space propagation until the wave strikes the front interface of the collimating lens. Also a second reflection occurs in this figure. This reflection is the response of the wave traveling through the front face of the lens, striking the back face at the exiting point of the lens, and reflecting back through the lens to the NWA. The third major reflection that can be noticed from this figure is the response from the metal plate, located at approximately 43 nanoseconds. One can further conclude that these components are indeed the causes of the responses by noting that there is no response coming from the second lens. All of the energy is reflected back by the metal plate and never reaches the second lens. In trying to solely focus on the response of a device under test, the response as a result of the reflection from the lens is a noticeable problem. The air/collimating lens match seems questionable and could use further investigation.

There are also multiple responses occurring in the data after the main response of the metal plate. This suggests that there could be a coupling issue with the system caused by ringing in the lenses or even multiple bounces between the lenses and the actual sample. Coupling issues are normally suggested to be mitigated using a time domain gating process [11]. However, a deeper concern is system multipath return that appears at the same time as the desired metal plate response. It is critical to note that this undesired multipath response cannot be gated out, and can therefore lead to gross-errors.

The distance between the focusing lens and the sample holder is reported to be 26.75 inches. With the mutipath effects that are noted in Figure 4.1, one can conclude that this may be an issue. At the lowest frequency (500MHz) the wavelength (23.6 inches) begins to approach the actual distance between these two components. At this wavelength, it may become electrically difficult to be able to distinguish between the two point scatterers, which could lead to a sample-lens coupling effect.

4.2   Time Domain Gated Data

As previously discussed, windowing causes data corruption in the low frequencies. To illustrate the need for a better approach, time domain gated data was taken for a fiberglass panel. The frequency range of this data is the full range of the LFFB system, 500MHz to 6GHz. A 2 nanosecond gate was used to mitigate any reflections outside of the plate reflection response. As can be noted in the upper plot of Figure 4.2, there is a high degree of variation present in the lower frequency range. The cause of this data corruption is commented on in Chapter 2. With the application of the three short calibration technique, some of the low frequency data should be recoverable. Also there is a roll off effect at the tail end of the data due to the data lost while applying the window in the frequency domain.

For completeness another set of windowed data was taken to show the effects of windowing in the extracted constitutive parameter data. In the bottom plot of Figure 4.2 a 1.25 nanosecond gate was applied. This set of data seems to be a little cleaner than the wider gate of 2 nanoseconds, but the obvious corruptions are still apparent. There are oscillations beginning from the low end of 500MHz and seemingly not settling until 2.3GHz. The roll off effect at the high frequency is still obvious.

4.3   Calibrated Constitutive Parameter Values of the Fiberglass Panel

With an understanding of the causes of system corruption and error, a detailed look at the calibrated results of a fiberglass panel may now be analyzed. The sample under test is 0.183 inches thick. It is a dielectric with an expected dielectric constant
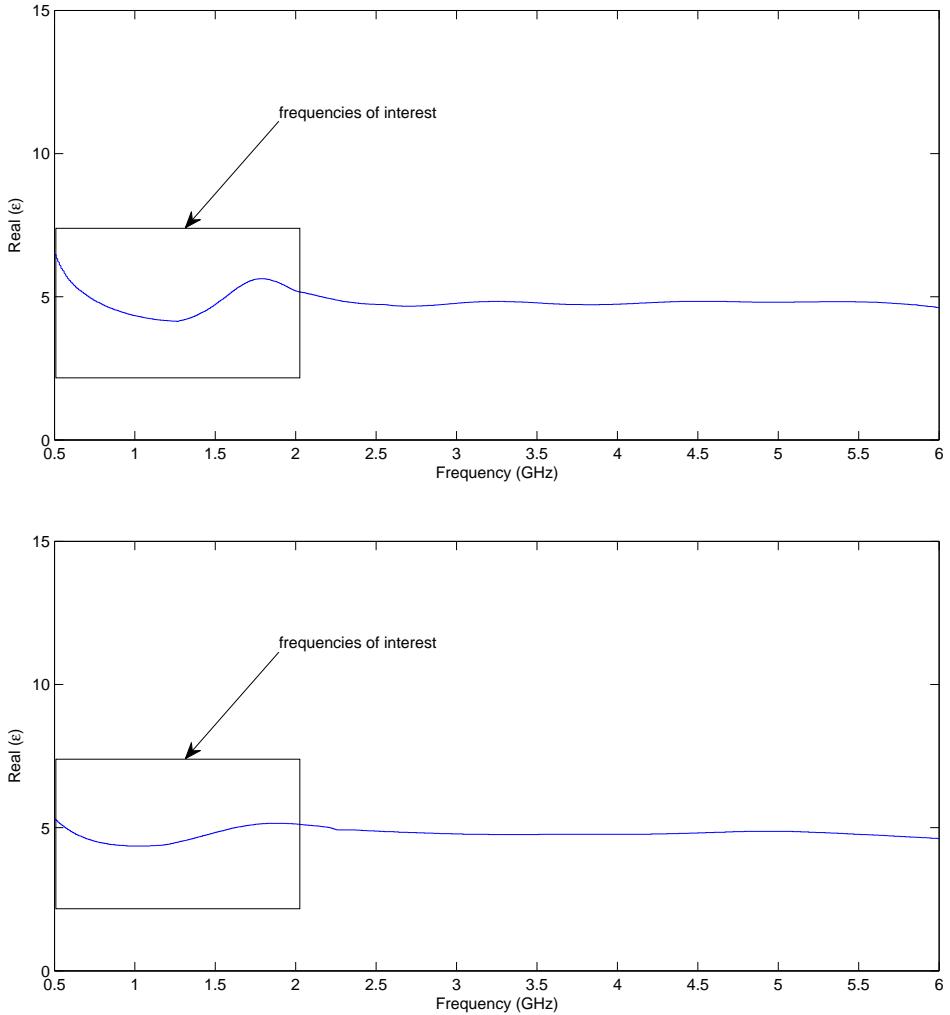
Figure 4.2: TE Incidence Permittivity Measurements. The top plot represents a an application of a 2 nanosecond gate. The bottom plot represents an application of a 1.25 nanosecond gate.

as noted from the time domain gated data of approximately 4.8. Plots of multiple material parameter extraction techniques are presented as a means of comparison.

The different approaches in calculating the material constitutive parameters will allow for better speculation of error within the data. Located on the plots are the derived data. These plots are created by use of the 1-Dimensional Newton-Raphson Root Search Algorithm, under the assumption that the material is non-magnetic. Theoretically, the S_{21} and S_{12} data should give better results because they are based

on information gained from material transmission data. This is due mainly to the fact that the precise location of calibration planes is extremely crucial. After translating the reflective standard during the calibration process, one can induce error into the results by not returning the sample holder to the initial $z = 0$ calibration plane. Investigation of this hypothesis is possible through analysis of the plots presented in Figure 4.3.

The next two plots depicted in Figure 4.3 are data extracted using the Nicolson Ross Weir Technique discussed in Chapter 2. One plot is generated by using the forward parameters S_{21} and S_{11}, and the other by using the reverse parameters S_{12} and S_{22}. This technique uses both reflection and transmission coefficients in order to extract the material constitutive parameter data. This technique may prove to be not as effective with this type of system because of the use of the reflection coefficient data.

Also, there are plots present to represent extraction by use of the 2-Dimensional Newton-Raphson Root Search Algorithm. This algorithm assumes no known knowledge of whether the material is a dielectric or not. They are added for completeness and should be noted that it also uses reflection coefficient data.

A numerical position independent complex material parameter extraction technique plot is also presented. This particular numerical method is an adaptation of the complex Newton-Raphson root search. The position independent formulation effectively eliminates any uncertainties in the sample position, which may prove to be the best parameter extraction technique.

In Figure 4.3, there are several details to be noted. The first detail is the corrupted data present in the 0.5GHz to 1GHz region. An aim of the three short calibration technique applied to this particular system was to be able to recover as much low end bandwidth data as possible. It is obvious that there are certain system imperfections in the low frequencies that were unable to be calibrated out with the use of this technique.
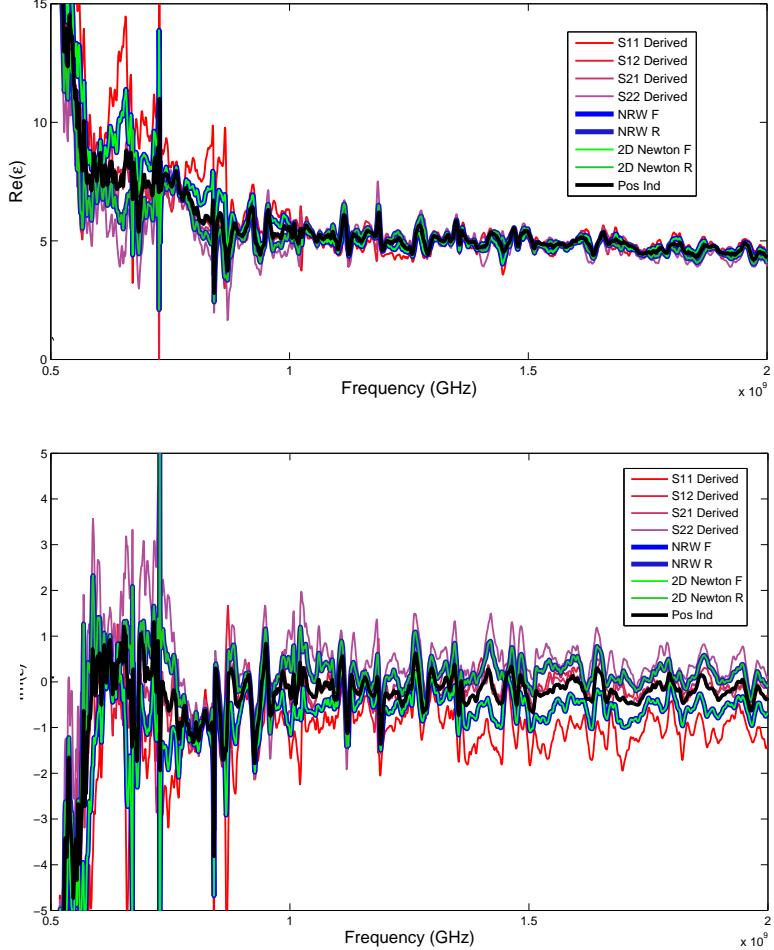
Figure 4.3: Real and Imaginary Extracted Components of the Fiberglass Panel Relative Permittivity

The cause of this can be related back to Figure 4.1. The initial reflections caused by the collimating and focusing lenses at these frequencies are calibrated out, but a coupling effect caused by the electromagnetic wave bouncing around within the lens was unable to be mitigated. The beam waist at these lower frequencies is also extremely wide, possibly causing other obstructions to be illuminated other than just the pure sample. The feed horns at these low frequencies also begin to perform rather poorly due to wide bandwidth. The data set that seems to have the lowest amplitude of variation is the position independent method.

44

As the frequency increases, the results become better. All of the different parameter extraction techniques seem to merge together and they converge towards the actual sample permittivity value. The noise that is visually still present in these frequencies could be due to a couple of factors. The first and most serious factor is that a high degree of accuracy when translating the three shorts is needed. The beam waist and poor performance of the horn can also be possible sources of error. Phase ambiguity may play a role in some of the lingering oscillations still present at the upper end of the bandwidth, but it is concluded that it is not a dominate source of error due to the fact that the results improve with increasing frequency.

The next plot to analyze is the imaginary component of the fiberglass panel. This panel is a dielectric and is assumed to be lossless. As depicted in the second plot of Figure 4.3, the imaginary component definitely converges to the expected value. Once again the position independent method seems to be the most accurate material parameter extraction technique for this system.

For completeness, the permeability of the dielectric panel is plotted. These results once again agree with our expected results. Once again as frequency increases, the parameter extraction techniques tend to converge to the same value. It is worth mentioning how the position independent method seems to be an averaging value of forward and reverse parameters. This phase shift between forward and reverse parameters is extremely evident in the lower frequencies. This can be caused by the sample holder not being returned with precision to the $z = 0$ plane. Nevertheless, the position independent extracts a value of 1 which is expected. The imaginary component of the permeability is 0, as anticipated

4.4 *Calibrated Constitutive Parameter Values of the Plexiglas Panel*

This section involves a similar analysis of a Plexiglas panel measured via the LFFB system. This Plexiglas panel is another known lossless dielectric, therefore the imaginary components are expected to be 0 and the theoretical relative permeability value should be 1.
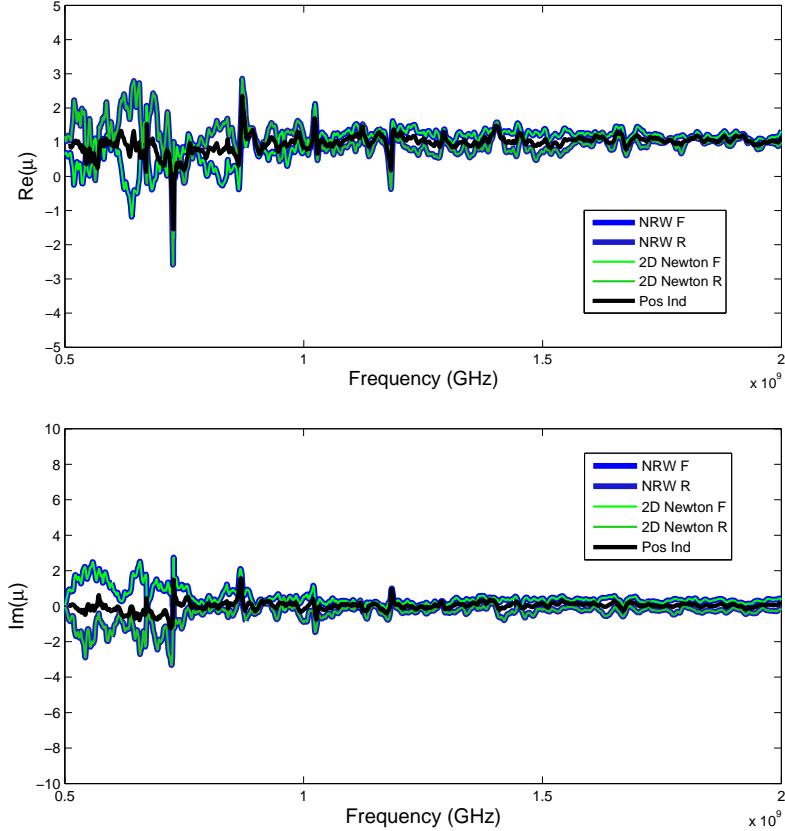
Figure 4.4:   Real and Imaginary Components of Fiberglass Permeability

Once again, it can be concluded for the sample that the coupling effects of multiple bounces within the lens and lens/sample interaction are two notable causes of significant error. The position independent method proves to be the most accurate of all the material parameter extraction techniques. As noted in the analysis of the fiberglass panel, all of the material parameter extraction techniques converge towards a common value as the frequency increases due to better system performance and less corrupted data in the reflection coefficients.

It is also worth mentioning that in the lower end of the bandwidth, the results obtained as compared to the fiberglass panel are less noisy. The Plexiglas sample theoretically has a lower dielectric constant than the fiberglass panel [2]. This means that the Plexiglas sample is more transmissive, therefore it should have less of a coupling effect with the focusing lens due to a smaller amount of energy being reflected

46
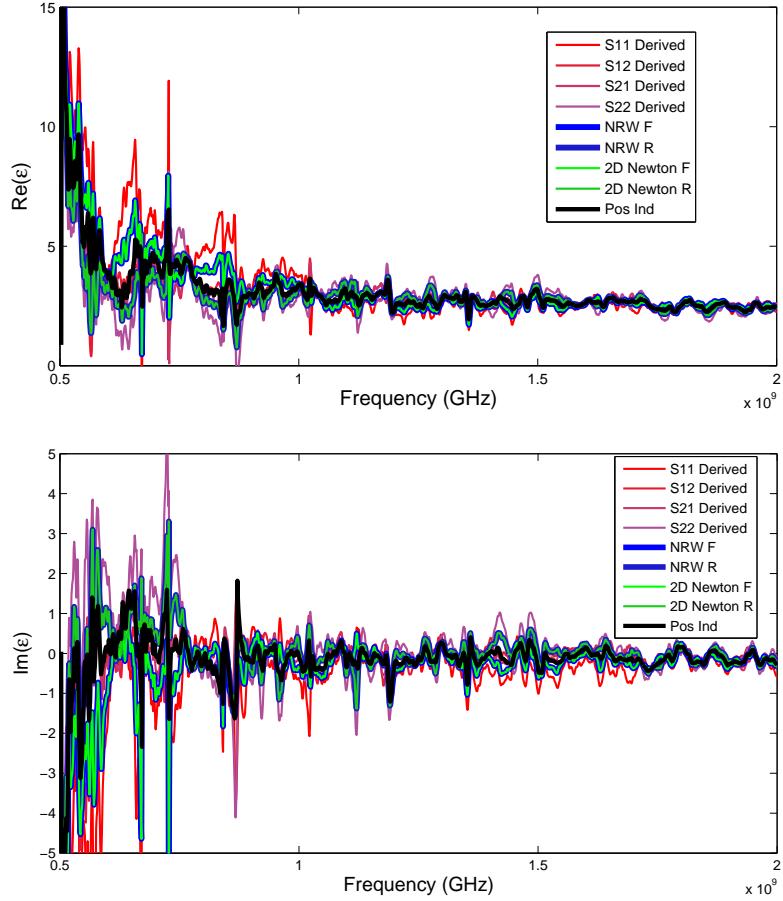
Figure 4.5:   Real and Imaginary Components of Plexiglass Permittivity

back. The results obtained confirm this, and suggest that a further investigation on the lens/sample interaction would be of interest.

4.5   Phase Ambiguity

The theory developed in Chapter Three suggests that there is a maximum spacing constraint that should help to eliminate degenerate errors in the calibration process. At the low end of the bandwidth, the smallest change in phase occurs, with a change of $\pm 36°$. This is theoretically an acceptable value and in reviewing the results obtained, it can be confirmed that phase ambiguity is not as big of a concern as compared to the inherent low frequency coupling effects of the system. If phase ambiguity was an issue, one would expect for the results to become more unstable as frequency

increases. This is due to the fact that with increasing frequency, wavelength becomes shorter and more precision is needed with shorter wavelengths than with longer ones. The results presented in Figures 4.3 and 4.5 show that phase ambiguity is not the main concern. The extracted data is better with increasing frequency, suggesting other causes of error.

4.6 Sample-Lens Coupling

With the results obtained not being as smooth as theoretically predicted, it is advantageous to explore the possibilities of the sources of error present. Taking a closer look at this data before it is processed through the extraction algorithms will give insight if the calibration was successful or not. In order to do this, the individual S-parameter components were separated. Similar to the process of time domain gating, an inverse Fourier transform was applied to the the calibrated S_{11} and S_{21}. The Matlab fftshift command was used to help visualize the transform with the 0 frequency component in the middle of the spectrum. In regards to post calibration, one would expect the multiple reflections caused by the lens in Figure 4.1 to be suppressed and the only response to be left is that of the actual sample. In reviewing Figure 4.6, it is evident that the multiple reflections noted in Figure 4.1 are suppressed. The three short calibration technique does an excellent job of mitigating all of the corruption that is present up until the point where the actual electromagnetic wave is incident upon the sample. However, it is clear that there are oscillations present directly after the main response of the actual sample that were not able to be calibrated out.

It can be concluded that these oscillations are the effects of coupling between the lens and the actual sample. At low frequencies where the wavelength is long, this can easily become a problem and there has yet to be a study to show how to counteract this interaction between the lens and the sample in free space systems without the use of time domain gating.
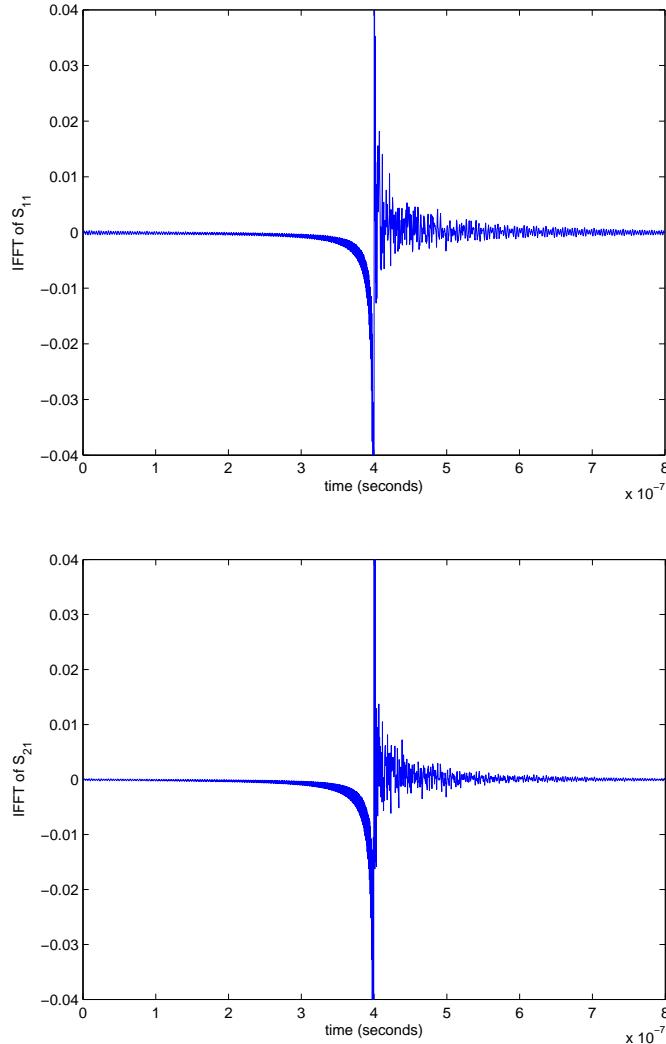
Figure 4.6:   The top graph represents the S_{11} response of the fiberglass sample post calibration. The bottom graph represents the S_{21} response of the fiberglass sample post calibration

In order to further confirm the hypothesis of coupling within the components of the system, an empty (air) post calibration measurement was taken. Theoretically, after calibration one would expect an S_{11} response of zero if there is not a device/sample under test in the sample holder. This is due to the fact that the calibration process aims to mitigate all extraneous sources of clutter, effectively isolating the backscatter from only the device/sample being measured. In the top plot of Figure 4.8, it is clearly seen that there is clutter in the lower end of the bandwidth that was not

49
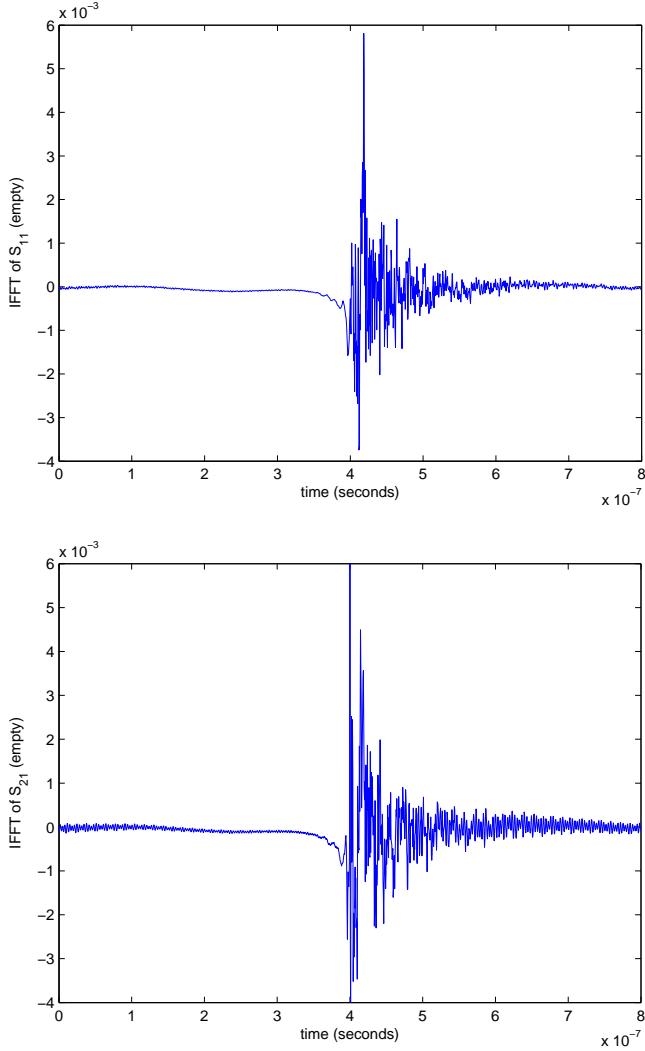
Figure 4.7: The top plot represents the calibrated time-domain S_{11} response of an empty "air" measurement. The bottom graph represents the calibrated time-domain S_{21} response of an empty "air" measurement.

accounted for during the calibration process. This clutter directly manifests itself within the sample data of interest. As frequency increases, the apparent corruption in the low frequencies becomes less apparent. This suggests that there are scattering phenomenons due to low frequency coupling between the metal plate used for calibration and the focusing lens that were not calibrated out.

Furthermore, one would expect an S_{21} response of one under the assumption that no energy is lost as the electromagnetic wave propagates through the system from

50

the transmitting antenna to the receiving antenna. In the bottom plot of Figure 4.8, the low frequency coupling phenomenon is once again shown. In correlation to the S_{11} response, this clutter phenomenon becomes less apparent as frequency increases. It is important to take a look at the phase shift caused by this low frequency coupling effect. In the lower end of the bandwidth as depicted in Figure 4.9, a peak phase shift of $\pm 3°$ is realized. This phase shift realized by an empty "air" measurement is an indicator that the sample data in this region will be corrupted. It is not until you get above 1GHz that an average phase shift of less than a degree is realized. Sliding window statistics are presented in Tables 4.3 and 4.4. These tables give a better insight into the clutter caused by this low frequency coupling effect inherent to the LFFB system.

In Figure 4.7, it is clear that the coupling effect caused by the lenses is not easily gated out. In both the S_{21} and S_{11} empty responses, there is a ringing effect that is not calibrated out that will cause the extracted sample constitutive parameter data to be corrupted.

4.7   Sample Size

The size of the sample being measured is an important factor. The phase difference produced by the sample is a function of its width and the frequency at which it is being tested. The resolution of the NWA becomes better as this phase difference increases. The phase angle as a function of frequency and sample width for both samples are plotted in Figure 4.10 and are derived from Equation (2.28). It can be suggested that the phase angles in the lower region of the bandwidth may not be enough for the NWA to completely resolve the signal from the noise floor. This phase problem theoretically diminishes with increasing frequency as the wavelengths become shorter and a higher phase difference is achieved. System coupling is still concluded to be the major source of error, but it is recommended that larger samples are used in future experimentation.

Table 4.2:   This table represents the extracted relative permittivity values of the fiberglass and plexiglas samples. Average and standard deviation values over 2 bandwidths were calculated using the position independent method.

	Fiberglass	Plexiglas
average ϵ_r (0.75-2GHz)	5.0959	2.7754
standard deviation (0.75-2GHz)	0.6083	0.3803
average ϵ_r (1GHz-2GHz)	4.9197	2.6647
standard deviation (1GHz-2GHz)	0.3373	0.2376

Table 4.3:   This table presents the phase statistics of a calibrated "air" measurement. The bandwidth of the experiment was split into 8 bins in order to view the average and variation over specific frequencies.

	S21		S12	
Frequency	mean	std	mean	std
500-687.5MHz	-0.1522	1.2723	-0.4527	1.1572
687.5-875MHz	-0.3770	0.6430	-0.2977	0.5422
875-1062.5MHz	-0.1237	0.4912	0.0822	0.5053
1.0625-1.25GHz	-0.0823	0.3440	-0.0935	0.3947
1.25-1.4375GHz	-0.0527	0.2114	-0.0692	0.2750
1.4375-1.625GHz	-0.0384	0.2330	-0.0530	0.2572
1.625-1.8125GHz	0.0190	0.1601	-0.0203	0.1724
1.8125-2GHz	-0.0376	0.1280	-0.0479	0.1408

Table 4.2 provides the extracted permittivity values of the fiberglass and plexiglas samples. Average values over two distinct bandwidths are provided to serve as a comparison to the extracted time domain gating method presented in Figure 4.2. Excluding the lower end of the bandwidth from 500MHz to 749MHz, results obtained agree with the theoretical values of the two dielectrics. Standard deviation values were calculated to represent the variation in data due to the low frequency coupling effects.

Table 4.4:   This table presents the magnitude statistics of a calibrated "air" measurement. The bandwidth of the experiment was split into 8 bins in order to view the average and variation over specific frequencies.

	S21		S12	
Frequency	mean	std	mean	std
500-687.5MHz	0.9931	0.0210	0.9948	0.0192
687.5-875MHz	1.0035	0.0109	0.9995	0.0087
875-1062.5MHz	1.0056	0.0081	1.0073	0.0067
1.0625-1.25GHz	0.9989	0.0060	0.9972	0.0064
1.25-1.4375GHz	1.0004	0.0037	1.0023	0.0044
1.4375-1.625GHz	0.9993	0.0041	0.9992	0.0045
1.625-1.8125GHz	0.9998	0.0028	0.9987	0.0027
1.8125-2GHz	1.0004	0.0023	1.0009	0.0024
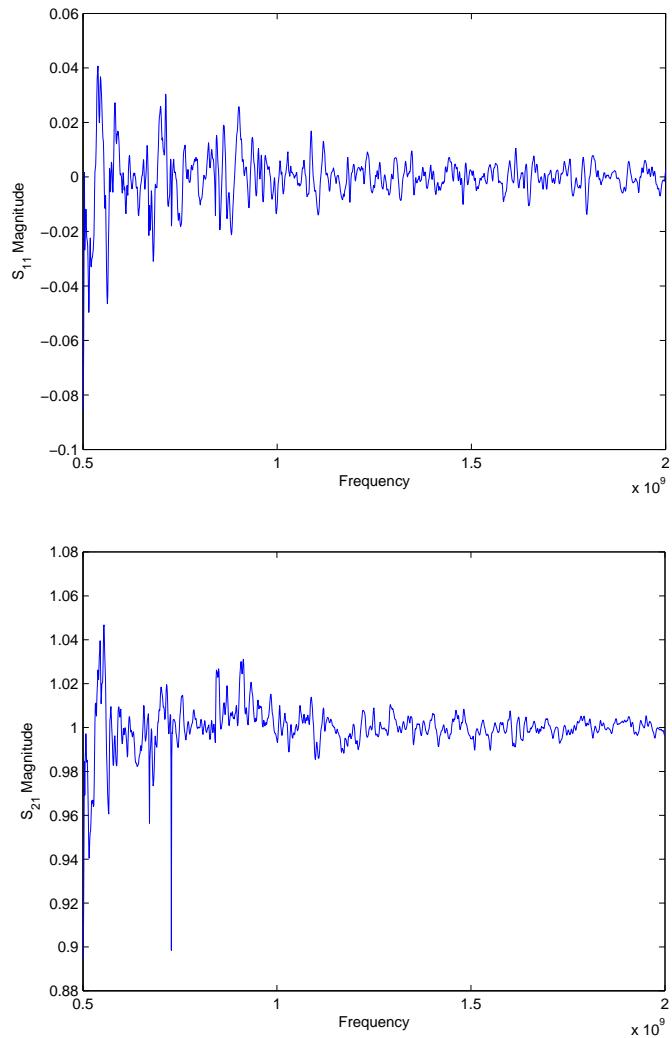
Figure 4.8:   The top plot represents a calibrated S_{11} response of an empty "air" measurement. The bottom plot represents a calibrated S_{21} response of an empty "air" measurement.
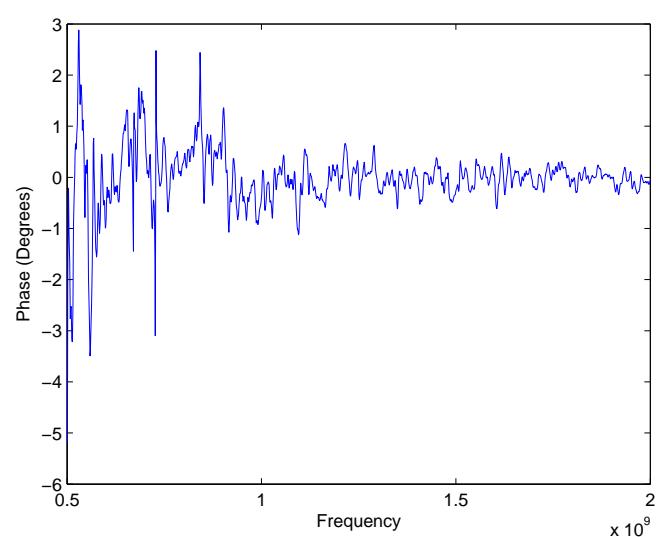
Figure 4.9:   This plot represents the phase shift caused by the low frequency coupling effect.
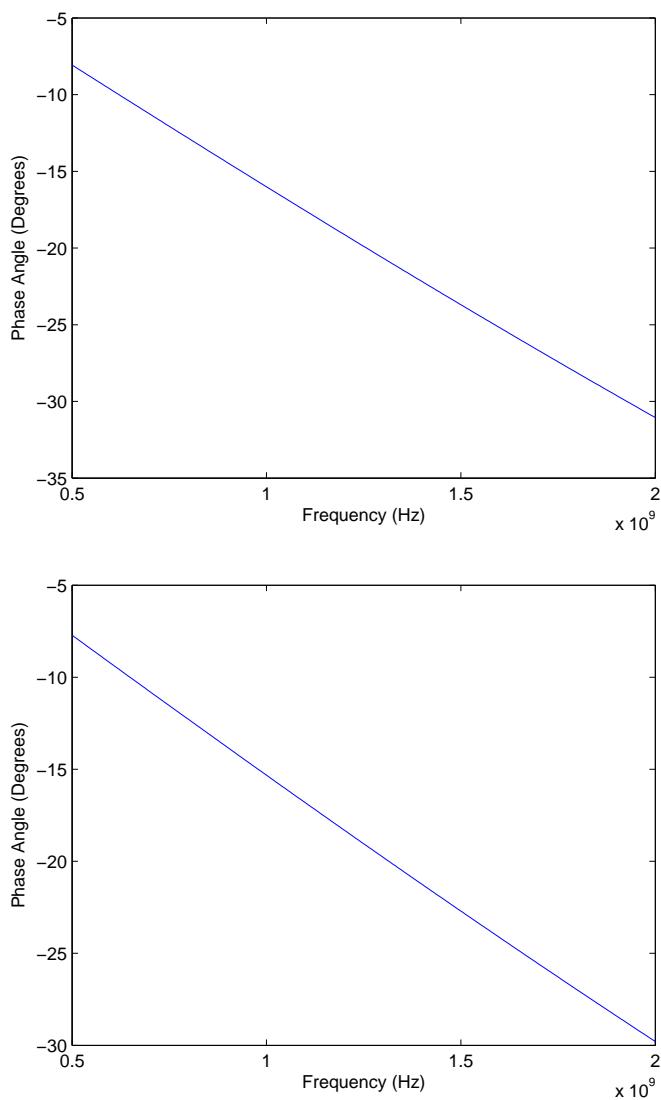
Figure 4.10: The top plot represents the phase angle difference realized by the 0.183 inch fiberglass sample. The bottom plot represents the phase angle difference realized by the 0.175 inch plexiglas sample.

V. Conclusions

The three short calibration technique was examined on a free space measurement system, the Low Frequency Focus Beam System. Although theory suggests that this technique is applicable, the results obtained suggest low frequency coupling between the multiple components of the system cause errors that are not easily calibrated out. Different numerical extraction techniques were used as a basis of comparison. The extracted constitutive parameters for both the Fiberglass sample and the Plexiglas sample, excluding the corrupted lower end of the bandwidth, on average were in agreement with the time domain gated data obtained by General Electric.

The main source of error within the results obtained is concluded to be caused by coupling effects within the system. By evaluating a post calibration empty (air) measurement, it is experimentally shown that there is a coupling effect associated with the dielectric lenses used to collimate and focus the electromagnetic wave onto the device under test. It is further shown by evaluation of the S_{11} and S_{22} responses of the dielectric samples, that there is also interaction between the sample and the lenses. This is validated because of the increased amplitude of oscillations as compared to the empty measurement. A position independent material parameter extraction algorithm proved to be the most accurate extraction technique as it nullified the phase differences between forward and reverse parameters. Although systematic errors were encountered, the average experimentally measured material parameter data obtained agreed with theoretically documented values.

5.1 Future Work

In order to utilize this technique on the Low Frequency Focus Beam System, a more precise way of translating the shorts in defining calibration planes is needed. Theory suggests that with precise definition of these calibration planes, accurate constitutive parameter data may be extracted. If the bandwidth of interest is 500MHz to 2GHz, separating the experiment into two bandwidth limits may prove to be useful. For example 500MHz-1.25GHZ and 1.25GHz-2GHz.

5.1.1   Quiet Zone and Reflective Standard.   A study can be conducted on the quiet zone of this system. This system is designed to where the energy is focused at the focal length of the focusing lens. By translating the short the maximum allowable distance, the energy distribution may become corrupted. Also more care can be taken when choosing the reflective standard. Literature states that less energy is reflected at lower frequencies. Polishing the standard would increase the reflected signal which would help separate the received signal from the noise floor of the system.

5.1.2   Sensitivity Analysis.   A quantitative study can be performed on how much error is induced into the system through improper calibration plane specification. The equations of the universal 12-term error model are well established. Altering each error term can be invoked in order to see which error terms cause the most error uncertainty within the results. With this information known, a more robust focus can be done on controlling the error associated with those terms.

5.1.3   FDTD Modeling.   In order to truly realize the source of the multiple reflections, a more extensive time domain modeling of the system should be investigated using the Finite Difference Time Domain technique.

Appendix A.   MatLab Code

The Matlab® code used to produce the plots in this thesis is presented. Multiple material parameter extraction techniques including the NRW and Newton-Raphson (1D, 2D, and Position Independent) were discussed and are placed in this Appendix for the purposes of reproducing results obtained in this thesis.

Listing A.1:   This file is the base file which contains functions to the various material parameter extraction techniques
(appendix1/WGunn_Thesis.m)

```matlab
function [] = WGunn_Thesis()

clear all; close all; clc

length_Sample_plexi =.00439412;
length_Sample_fg =.004648199999995;
K_csq =0;

% Parameter guesses
mu_plexi = 1 - 0.001j;
epsilon_plexi = 2.8 - 0.001j;

mu_fg = 1 - .001j;
epsilon_fg = 4.86 - 0.001j;

% Determine the S-parameters for Plexiglass and Fiberglass
[material_Measurements] = getLabData();
Freq = material_Measurements(:,1);
S21_1 = material_Measurements(:,2);
S11_1 = material_Measurements(:,3);
S12_1 = material_Measurements(:,4);
S22_1 = material_Measurements(:,5);

[material_Measurements] = getLabData();
Freq = material_Measurements(:,1);
S21_2 = material_Measurements(:,2);
S11_2 = material_Measurements(:,3);
S12_2 = material_Measurements(:,4);
S22_2 = material_Measurements(:,5);



C = 2.997925e8;
mu_0 = pi*4e-7;
epsilon_0 = 1/(C^2*mu_0);

K_osq = (2*pi.*Freq).^2.*epsilon_0.*mu_0;
gamma_o = sqrt(K_csq - K_osq);
```

```matlab
41 K_o = sqrt(K_osq);

   S22_1=S22_1.*exp(-1i*2.*K_o*length_Sample_plexi);
   S21_1=S21_1.*exp(-1i.*K_o*length_Sample_plexi);
   S12_1=S12_1.*exp(-1i.*K_o*length_Sample_plexi);
46
   S22_2=S22_2.*exp(-1i*2.*K_o*length_Sample_fg);
   S21_2=S21_2.*exp(-1i.*K_o*length_Sample_fg);
   S12_2=S12_2.*exp(-1i.*K_o*length_Sample_fg);


51

   % Use the NRW method to compute the Plexiglass and Ram material ...
       parameters
   [mu_rel_forward_1 , epsilon_rel_forward_1] = computeNRW(S11_1, ...
       S21_1 ,...
       gamma_o , length_Sample_plexi , K_csq , K_osq);
56 [mu_rel_reverse_1 , epsilon_rel_reverse_1] = computeNRW(S22_1, ...
       S12_1 ,...
       gamma_o , length_Sample_plexi , K_csq , K_osq);

   [mu_rel_forward_2 , epsilon_rel_forward_2] = computeNRW(S11_2, ...
       S21_2 ,...
       gamma_o , length_Sample_fg , K_csq , K_osq);
61 [mu_rel_reverse_2 , epsilon_rel_reverse_2] = computeNRW(S22_2, ...
       S12_2 ,...
       gamma_o , length_Sample_fg , K_csq , K_osq);



   % Use 1D and 2D Newton-Raphson complex root search method
66 [epsilon_S11_plexi] = newtonRootSearchS11(Freq,length_Sample_plexi...
       ,...
       S11_1, K_csq , mu_plexi , epsilon_plexi);
   [epsilon_S22_plexi] = newtonRootSearchS11(Freq,length_Sample_plexi...
       ,...
       S22_1, K_csq , mu_plexi , epsilon_plexi);
   [epsilon_S21_plexi] = newtonRootSearchS21(Freq,length_Sample_plexi...
       ,...
71     S21_1, K_csq , mu_plexi , epsilon_plexi);
   [epsilon_S12_plexi] = newtonRootSearchS21(Freq,length_Sample_plexi...
       ,...
       S12_1, K_csq , mu_plexi , epsilon_plexi);

   [epsilon_S11_fg] = newtonRootSearchS11(Freq,length_Sample_fg ,...
76     S11_2, K_csq , mu_fg , epsilon_fg);
   [epsilon_S22_fg] = newtonRootSearchS11(Freq,length_Sample_fg ,...
       S22_2, K_csq , mu_fg , epsilon_fg);
   [epsilon_S21_fg] = newtonRootSearchS21(Freq,length_Sample_fg ,...
       S21_2, K_csq , mu_fg , epsilon_fg);
81 [epsilon_S12_fg] = newtonRootSearchS21(Freq,length_Sample_fg ,...
       S12_2, K_csq , mu_fg , epsilon_fg);
```

```matlab
    [epsilon_f_plexi1,mu_f_plexi1] = newtonRootSearch2D(Freq,...
        length_Sample_plexi, S11_1, S21_1, mu_plexi, epsilon_plexi,...
            K_csq);
86  [epsilon_r_plexi1,mu_r_plexi1] = newtonRootSearch2D(Freq,...
        length_Sample_plexi, S22_1, S12_1, mu_plexi, epsilon_plexi,...
            K_csq);
    [epsilon_f_fg1,mu_f_fg1] = newtonRootSearch2D(Freq, ...
        length_Sample_fg, S11_2, S21_2, mu_fg, epsilon_fg,K_csq);
    [epsilon_r_fg1,mu_r_fg1] = newtonRootSearch2D(Freq, ...
91      length_Sample_fg, S22_2, S12_2, mu_fg, epsilon_fg,K_csq);

    % Use position independent 2D Newton-Raphson method
    [epsilon_plexi2, mu_plexi2] = posIndependent(Freq, ...
        length_Sample_plexi,...
            S11_1, S12_1, S21_1, S22_1, mu_plexi, epsilon_plexi,K_csq);
96  [epsilon_fg2, mu_fg2] = posIndependent(Freq, length_Sample_fg,...
        S11_2, S12_2, S21_2, S22_2, mu_fg, epsilon_fg,K_csq);




101
    % Display all the plexiglass parameters
    scrsz = get(0,'ScreenSize');
    h1 = figure('Name','Real Component Plexiglass Permittivity','...
        Position',...
            [1 scrsz(4)/2 scrsz(3)/2 scrsz(4)/2]);
106 plot(Freq, real(epsilon_S11_plexi),'LineWidth',1.5,'color'...
        ,[1,0,0]); hold on
    plot(Freq, real(epsilon_S12_plexi),'LineWidth',1.5,'color'...
        ,[.9,0.1,0.2]); hold on
    plot(Freq, real(epsilon_S21_plexi),'LineWidth',1.5,'color'...
        ,[.8,0.2,0.4]); hold on
    plot(Freq, real(epsilon_S22_plexi),'LineWidth',1.5,'color'...
        ,[.7,0.3,0.6]); hold on
    plot(Freq, real(epsilon_rel_forward_1),'LineWidth',4,'color'...
        ,[0,0,1]); hold on
111 plot(Freq, real(epsilon_rel_reverse_1),'LineWidth',4,'color'...
        ,[.1,.1,.8]); hold on
    plot(Freq, real(epsilon_f_plexi1),'LineWidth',1.5,'color',[0,1,0])...
        ;hold on
    plot(Freq, real(epsilon_r_plexi1),'LineWidth',1.5,'color'...
        ,[.1,.8,.1]); hold on
    plot(Freq, real(epsilon_plexi2),'LineWidth',3,'color',[0,0,0])
    ylim([0 15])
116 xlabel('Frequency (GHz)','FontSize',14);
    ylabel('Re(\epsilon)', 'FontSize', 14);
    legend('S11 Derived','S12 Derived','S21 Derived','S22 Derived','...
        NRW F',...
            'NRW R','2D Newton F','2D Newton R','Pos Ind',3)

121 h2 = figure('Name','Imaginary Component Plexiglass Permittivity','...
        Position',...
```

```matlab
            [1 scrsz(4)/2 scrsz(3)/2 scrsz(4)/2]);
        plot(Freq, imag(epsilon_S11_plexi),'LineWidth',1.5,'color'...
            ,[1,0,0]); hold on
        plot(Freq, imag(epsilon_S12_plexi),'LineWidth',1.5,'color'...
            ,[.9,0.1,0.2]); hold on
        plot(Freq, imag(epsilon_S21_plexi),'LineWidth',1.5,'color'...
            ,[.8,0.2,0.4]); hold on
126     plot(Freq, imag(epsilon_S22_plexi),'LineWidth',1.5,'color'...
            ,[.7,0.3,0.6]); hold on
        plot(Freq, imag(epsilon_rel_forward_1),'LineWidth',4,'color'...
            ,[0,0,1]); hold on
        plot(Freq, imag(epsilon_rel_reverse_1),'LineWidth',4,'color'...
            ,[.1,.1,.8]); hold on
        plot(Freq, imag(epsilon_f_plexi1),'LineWidth',1.5,'color',[0,1,0])...
            ; hold on
        plot(Freq, imag(epsilon_r_plexi1),'LineWidth',1.5,'color'...
            ,[.1,.8,.1]); hold on
131     plot(Freq, imag(epsilon_plexi2),'LineWidth',3,'color',[0,0,0])
        ylim([-5 5])
        xlabel('Frequency (GHz)','FontSize',14);
        ylabel('Im(\epsilon)', 'FontSize', 14);
        legend('S11 Derived','S12 Derived','S21 Derived','S22 Derived','...
            NRW F',...
136         'NRW R','2D Newton F','2D Newton R','Pos Ind',3)

        h3 = figure('Name','Real Component Plexiglass Permeability','...
            Position',...
            [1 scrsz(4)/2 scrsz(3)/2 scrsz(4)/2]);
        plot(Freq, real(mu_rel_forward_1),'LineWidth',4,'color',[0,0,1]); ...
            hold on
141     plot(Freq, real(mu_rel_reverse_1),'LineWidth',4,'color'...
            ,[.1,.1,.8]); hold on
        plot(Freq, real(mu_f_plexi1),'LineWidth',1.5,'color',[0,1,0]) ;...
            hold on
        plot(Freq, real(mu_r_plexi1),'LineWidth',1.5,'color',[.1,.8,.1]); ...
            hold on
        plot(Freq, real(mu_plexi2),'LineWidth',3,'color',[0,0,0])
        ylim([-5 5])
146     xlabel('Frequency (GHz)','FontSize',14);
        ylabel('Re(\mu)', 'FontSize', 14);
        legend('NRW F','NRW R','2D Newton F','2D Newton R','Pos Ind',3)

        h4 = figure('Name','Imaginary Component Plexiglass Permeability','...
            Position',...
151         [1 scrsz(4)/2 scrsz(3)/2 scrsz(4)/2]);
        plot(Freq, imag(mu_rel_forward_1),'LineWidth',4,'color',[0,0,1]); ...
            hold on
        plot(Freq, imag(mu_rel_reverse_1),'LineWidth',4,'color'...
            ,[.1,.1,.8]); hold on
        plot(Freq, imag(mu_f_plexi1),'LineWidth',1.5,'color',[0,1,0]); ...
            hold on
```

```
     plot(Freq, imag(mu_r_plexi1),'LineWidth',1.5,'color',[.1,.8,.1]); ...
         hold on
156 plot(Freq, imag(mu_plexi2),'LineWidth',3,'color',[0,0,0])
    ylim([-10 10])
    xlabel('Frequency (GHz)','FontSize',14);
    ylabel('Im(\mu)', 'FontSize', 14);
    legend('NRW F','NRW R','2D Newton F','2D Newton R','Pos Ind',3)
161


    % Display all the RAM parameters
    h5 = figure('Name','Real Component Fiberglass Permittivity','...
        Position',...
166       [1 scrsz(4)/2 scrsz(3)/2 scrsz(4)/2]);
    plot(Freq, real(epsilon_S11_fg),'LineWidth',1.5,'color',[1,0,0]); ...
         hold on
    plot(Freq, real(epsilon_S12_fg),'LineWidth',1.5,'color'...
         ,[.9,0.1,0.2]); hold on
    plot(Freq, real(epsilon_S21_fg),'LineWidth',1.5,'color'...
         ,[.8,0.2,0.4]); hold on
    plot(Freq, real(epsilon_S22_fg),'LineWidth',1.5,'color'...
         ,[.7,0.3,0.6]); hold on
171 plot(Freq, real(epsilon_rel_forward_2),'LineWidth',4,'color'...
         ,[0,0,1]); hold on
    plot(Freq, real(epsilon_rel_reverse_2),'LineWidth',4,'color'...
         ,[.1,.1,.8]); hold on
    plot(Freq, real(epsilon_f_fg1),'LineWidth',1.5,'color',[0,1,0]); ...
         hold on
    plot(Freq, real(epsilon_r_fg1),'LineWidth',1.5,'color',[.1,.8,.1])...
         ; hold on
    plot(Freq, real(epsilon_fg2),'LineWidth',3,'color',[0,0,0])
176 ylim([0 15])
    xlabel('Frequency (GHz)','FontSize',14);
    ylabel('Re(\epsilon)', 'FontSize', 14);
    legend('S11 Derived','S12 Derived','S21 Derived','S22 Derived','...
        NRW F',...
         'NRW R','2D Newton F','2D Newton R','Pos Ind',3)
181

    h6 = figure('Name','Imaginary Component Fiberglass Permittivity','...
        Position',...
         [1 scrsz(4)/2 scrsz(3)/2 scrsz(4)/2]);
    plot(Freq, imag(epsilon_S11_fg),'LineWidth',1.5,'color',[1,0,0]); ...
         hold on
186 plot(Freq, imag(epsilon_S12_fg),'LineWidth',1.5,'color'...
         ,[.9,0.1,0.2]); hold on
    plot(Freq, imag(epsilon_S21_fg),'LineWidth',1.5,'color'...
         ,[.8,0.2,0.4]); hold on
    plot(Freq, imag(epsilon_S22_fg),'LineWidth',1.5,'color'...
         ,[.7,0.3,0.6]); hold on
    plot(Freq, imag(epsilon_rel_forward_2),'LineWidth',4,'color'...
         ,[0,0,1]); hold on
```

```matlab
    plot(Freq, imag(epsilon_rel_reverse_2),'LineWidth',4,'color'...
        ,[.1,.1,.8]); hold on
191 plot(Freq, imag(epsilon_f_fg1),'LineWidth',1.5,'color',[0,1,0]); ...
        hold on
    plot(Freq, imag(epsilon_r_fg1),'LineWidth',1.5,'color',[.1,.8,.1])...
        ; hold on
    plot(Freq, imag(epsilon_fg2),'LineWidth',3,'color',[0,0,0])
    ylim([-5 5])
    xlabel('Frequency (GHz)','FontSize',14);
196 ylabel('Im(\epsilon)', 'FontSize', 14);
    legend('S11 Derived','S12 Derived','S21 Derived','S22 Derived','...
        NRW F',...
         'NRW R','2D Newton F','2D Newton R','Pos Ind',3)


201 h7 = figure('Name','Real Component Fiberglass Permeability','...
        Position',...
         [1 scrsz(4)/2 scrsz(3)/2 scrsz(4)/2]);
    plot(Freq, real(mu_rel_forward_2),'LineWidth',4,'color',[0,0,1]); ...
        hold on
    plot(Freq, real(mu_rel_reverse_2),'LineWidth',4,'color'...
        ,[.1,.1,.8]); hold on
    plot(Freq, real(mu_f_fg1),'LineWidth',1.5,'color',[0,1,0]); hold ...
        on
206 plot(Freq, real(mu_r_fg1),'LineWidth',1.5,'color',[.1,.8,.1]); ...
        hold on
    plot(Freq, real(mu_fg2),'LineWidth',3,'color',[0,0,0])
    ylim([-5 5])
    xlabel('Frequency (GHz)','FontSize',14);
    ylabel('Re(\mu)', 'FontSize', 14);
211 legend('NRW F','NRW R','2D Newton F','2D Newton R','Pos Ind',3)

    h8 = figure('Name','Imaginary Component Fiberglass Permeability','...
        Position',...
         [1 scrsz(4)/2 scrsz(3)/2 scrsz(4)/2]);
    plot(Freq, imag(mu_rel_forward_2),'LineWidth',4,'color',[0,0,1]); ...
        hold on
216 plot(Freq, imag(mu_rel_reverse_2),'LineWidth',4,'color'...
        ,[.1,.1,.8]); hold on
    plot(Freq, imag(mu_f_fg1),'LineWidth',1.5,'color',[0,1,0]); hold ...
        on
    plot(Freq, imag(mu_r_fg1),'LineWidth',1.5,'color',[.1,.8,.1]); ...
        hold on
    plot(Freq, imag(mu_fg2),'LineWidth',3,'color',[0,0,0])
    ylim([-10 10])
221 xlabel('Frequency (GHz)','FontSize',14);
    ylabel('Im(\mu)', 'FontSize', 14);
    legend('NRW F','NRW R','2D Newton F','2D Newton R','Pos Ind',3)

    end
```

Listing A.2:   This file allows the data obtained from the NWA to be imported into matlab.

(appendix1/getLabData.m)

```matlab
% Network Anaylzer Data Importer
% Lt William Gunn
%
% [Material_Measurements] = getLabData(inputFile) imports data ...
      files from
5 % the network analyzer in the materials lab into a single matrix ...
      with each
% column representing frequency, S11, S12, S21, S22.  The optional...
       argument
% FILENAME is a string that contains the path and name of the data...
       file in
% the format DRIVE_LETTER:\DIRECTORY\...\DIRECTORY\FILENAME.CTI.  ...
      If
% FILENAME isn't specified, the user will be prompted to specify ...
      the file
10 % with an open-file dialog box.

   function [Material_Measurements] = getLabData(inputFile)

   %Allow the user to select the files to import if not specified
15 if nargin ~= 0
       fid = fopen(inputFile);
   elseif (nargin==0)||(fid==-1)
       [impfilenm, impfilepath] = uigetfile({'*.cti','CTI Files (*....
           cti)';...
            '*.txt','Text Files (*.txt)';'*.*','All Files (*.*)'},'...
                Select Data File for Import');
20     fid = fopen([impfilepath impfilenm]);
   end

   % Scan the file and extract pertinent information.  Setting the ...
      headerlines
   % eliminates the entire header such that it begins with the ...
      frequency
25 C_Data = textscan(fid, '%s', 'headerlines');

   % This undoes the strange cell-within-a-cell output that textscan ...
      uses
   C_Data = C_Data{:};

30 % Splits the column for S-parameters into a real and imaginary ...
      column
   [C_Data(:,1), C_Data(:,2)] = strtok(C_Data,',');

   % Locate the end of the file heading
   data_Begin = strmatch('VAR_LIST_BEGIN',C_Data);
35
```

65

```matlab
  % Locate the beginning of each data column and define column ...
      length
  Data_Cells = strmatch('BEGIN',C_Data);
  C_Length = Data_Cells(1) - data_Begin - 2;
40
  % Preallocate variables for Freq, S11, S12, S21, S22
  var_Meas = length(Data_Cells) + 1;
  Measurements = nan([C_Length, var_Meas]);


45
  %Fill measurements array with Frequency, S11, S12, S21, S22

  Measurements(:,1) = str2double(C_Data((data_Begin + 1):(C_Length +...
      data_Begin)));
  parfor i = 1:length(Data_Cells)
50    Measurements(:,i+1) = str2double(C_Data(Data_Cells(i) + 1: ...
        Data_Cells(i) + C_Length,1))+ j.*str2double(C_Data(...
        Data_Cells(i) + 1: Data_Cells(i) + C_Length,2));
  end

  %Close the data file
  fclose(fid);
55
  %Pass extracted information out
  Material_Measurements = Measurements;

  end
```

Listing A.3:   This file uses the Nicolson-Ross-Weir material parameter extraction technique

(appendix1/computeNRW.m)

```matlab
1 % NRW Method Computation
  % Lt William Gunn

  function [mu_rel, epsilon_rel] = computeNRW(S11_22, S21_12, ...
      gamma_o, ...
       length_Sample, K_csq, K_osq)
6


  % Calculate values for Q
  Q = (S11_22.^2 - S21_12.^2 + 1)./(2.*S11_22);
11
  % Calculate R and determine proper root choice
  R_pos = Q + sqrt(Q.^2 - 1);
  R_neg = Q - sqrt(Q.^2 - 1);
  R = (abs(R_pos)<=1).*R_pos + (abs(R_neg)<=1).*R_neg;
16
  % Calculate values for P
  P = S21_12./(1 - R.*S11_22);

  % Calculate the sample relative permittivity and permeability
```

```
21 mu_rel = (-log(P)./(gamma_o.*length_Sample)).*((1 + R)./(1 - R));
   epsilon_rel = (K_csq - (log(P)./length_Sample).^2)./(K_osq.*mu_rel...
       );
```

Listing A.4:   This file uses the Newton-Raphson 1D material parameter extraction technique. This technique assumes that the material is either a dielectric or purely magnetic. The reflection coefficients are used to extract material constitutive parameters.

```
   % Complex Newton Root Search
   % Lt William Gunn
 3 %
   % The newtonRootSearch1D() function numerically seeks the complex
   % permittivity for each S-Parameter.


 8 function [epsilon_S11] = newtonRootSearchS11(Freq,length_Sample,...
       S11_meas,...
         K_csq, mu_rel, epsilon_rel)

   % Initialize constants
   tol = 10^(-7);
13 eps = 1;
   k = 0;

   delta = 1e-7;

18 x = mu_rel;

   y = epsilon_rel;

   dy = y + delta;
23

   while ((eps > tol) && (k < 100))
       % Compute the theoretical S-parameters
       [S11_22_thy] = computeS11Parameter(Freq,length_Sample,x,y,...
           K_csq);
28     [S11_22_thy_dy] = computeS11Parameter(Freq,length_Sample,x,dy,...
           K_csq);

       % Define the standard functions
       F = S11_22_thy - S11_meas;

33     % Define the derivative functions
       F_dy = S11_22_thy_dy - S11_meas;

       dFy = (F_dy - F)./delta;

38     % Calculate next permittivity guess
       yn = y - F./dFy;
```

```matlab
        % Find the lowest relative approximate error
        eps = min(abs((yn - y)));
43
        % Set the new permittivity guess
        y = yn;

        % Calculate the new deltas
48      % delta = -F./dFy;

        dy = y + delta;

        k = k + 1;
53  end

    % Pass the relative permittivites out for each S-parameter
    epsilon_S11 = y;
```

Listing A.5: This file uses the Newton-Raphson 1D material parameter extraction technique. This technique assumes that the material is either a dielectric or purely magnetic. The transmission coefficients are used to extract material constitutive parameters.

(appendix1/newtonRootSearchS21.m)

```matlab
% Complex Newton Root Search
% Lt William Gunn
%
4 % The newtonRootSearch1D() function numerically seeks the complex
% permittivity for each S-Parameter.


  function [epsilon_S21] = newtonRootSearchS21(Freq,length_Sample,...
     S21_meas,...
9     K_csq, mu_rel, epsilon_rel)

  % Initialize constants
  tol = 10^(-7);
  eps = 1;
14 k = 0;

  delta = 1e-7;

  x = mu_rel;
19
  y = epsilon_rel;

  dy = y + delta;


24
  while ((eps > tol) && (k < 100))
      % Compute the theoretical S-parameters
```

68

```matlab
        [S21_12_thy] = computeS21Parameter(Freq,length_Sample,x,y,...
            K_csq);
        [S21_12_thy_dy] = computeS21Parameter(Freq,length_Sample,x,dy,...
            K_csq);

        % Define the standard functions
        F = S21_12_thy - S21_meas;

        % Define the derivative functions
        F_dy = S21_12_thy_dy - S21_meas;

        dFy = (F_dy - F)./delta;

        % Calculate next permittivity guess
        yn = y - F./dFy;

        % Find the lowest relative approximate error
        eps = min(abs((yn - y)));

        % Set the new permittivity guess
        y = yn;

        % Calculate the new deltas
        % delta = -F./dFy;

        dy = y + delta;

        k = k + 1;
    end

% Pass the relative permittivites out for each S-parameter
epsilon_S21 = y;
```

Listing A.6:   This file uses the Newton-Raphson 2D material parameter extraction technique. This technique assumes that the user does not know the material constitutive parameters. The reflection and transmission coefficients are used to solve two equations with two unknowns to extract material constitutive parameters.
(appendix1/newtonRootSearch2D.m)

```matlab
% Position Independent Analysis
% Lt William Gunn
% 2-Dimensional Newton Root Search Method


function [epsilon, mu] = newtonRootSearch2D(Freq,length_Sample,...
    S11_meas, S21_meas, x, y, K_csq)


% Initialize constants
tol = 10^(-7);
eps = 1;
k = 0;
```

```matlab
14  delta = 10^(-7);

    dx = x + delta;
    dy = y + delta;

19
    while ((eps > tol) && (k < 100))
        % Get S-parameters for standard and derivative functions
        [S11_22_thy] = computeS11Parameter(Freq,length_Sample,x,y,...
            K_csq);
        [S21_12_thy] = computeS21Parameter(Freq,length_Sample,x,y,...
            K_csq);
24      [S11_22_thy_dy] = computeS11Parameter(Freq,length_Sample,x,dy,...
            K_csq);
        [S21_12_thy_dy] = computeS21Parameter(Freq,length_Sample,x,dy,...
            K_csq);
        [S11_22_thy_dx] = computeS11Parameter(Freq,length_Sample,dx,y,...
            K_csq);
        [S21_12_thy_dx] = computeS21Parameter(Freq,length_Sample,dx,y,...
            K_csq);

29      % Define the standard functions
        F = S11_22_thy - S11_meas;
        G = S21_12_thy - S21_meas;

        % Define the derivative functions
34      F_dy = S11_22_thy_dy - S11_meas;
        G_dy = S21_12_thy_dy - S21_meas;

        F_dx = S11_22_thy_dx - S11_meas;
        G_dx = S21_12_thy_dx - S21_meas;
39
        % Compute the partial dervatives
        dFy = (F_dy - F)./delta;
        dGy = (G_dy - G)./delta;

44      dFx = (F_dx - F)./delta;
        dGx = (G_dx - G)./delta;

        % Calculate next permittivity and permeability guess
        xn = x - (1./(dFx.*dGy - dFy.*dGx).*(F.*dGy - dFy.*G));
49      yn = y - (1./(dFx.*dGy - dFy.*dGx).*(-F.*dGx + dFx.*G));

        % Find the lowest relative approximate error
        eps1 = max(abs((sqrt(xn) - x)));
        eps2 = max(abs((sqrt(yn) - y)));
54
        eps = max([eps1 eps2]);

        % Set the new permittivity and permeability guesses
        x = xn;
59      y = yn;
```

70

```
        dy = y + delta;
        dx = x + delta;

64      k = k + 1;
    end

    % Pass out the relative permittivites and permeabilities
    epsilon = y;
69  mu = x;
```

Listing A.7: This file uses a variation of the Newton-Raphson 2D root search algorithm. This file allows for position independence.
(appendix1/posIndependent.m)

```
 1 % Position Independent Analysis
   % Lt William Gunn
   %
   % The posIndependent() function numerically seeks the complex
   % permittivity and permeability for the given S-Parameters ...
       regardless of
 6 % sample position.


   function [epsilon, mu] = posIndependent(Freq,length_Sample,...
       S11_meas, S12_meas, S21_meas, S22_meas, x, y,K_csq)
11

   % Initialize constants
   tol = 10^(-7);
   conv = 1;
16 k = 0;

   delta = 10^(-7);

   dx = x + delta;
21 dy = y + delta;


   while ((conv > tol) && (k < 100))
       % Get S-parameters for standard and derivative functions
26     [S11_22_thy, S21_12_thy] = computeSParameter(Freq,...
           length_Sample,x,y,K_csq);

       [S11_22_thy_dy,S21_12_thy_dy] = computeSParameter(Freq,...
           length_Sample,x,dy,K_csq);
       [S11_22_thy_dx,S21_12_thy_dx] = computeSParameter(Freq,...
           length_Sample,dx,y,K_csq);

31     % Define the standard functions
       F = S21_12_thy.^2 - S21_meas.*S12_meas;
       G = S11_22_thy.^2 - S11_meas.*S22_meas;
```

71

```matlab
      % Define the derivative functions
36    F_dy = S21_12_thy_dy.^2 - S21_meas.*S12_meas;
      G_dy = S11_22_thy_dy.^2 - S11_meas.*S22_meas;

      F_dx = S21_12_thy_dx.^2 - S21_meas.*S12_meas;
      G_dx = S11_22_thy_dx.^2 - S11_meas.*S22_meas;
41
      % Compute the partial dervatives
      dFy = (F_dy - F)./delta;
      dGy = (G_dy - G)./delta;

46    dFx = (F_dx - F)./delta;
      dGx = (G_dx - G)./delta;

      % Calculate next permittivity and permeability guess
      xn = x - (1./(dFx.*dGy - dFy.*dGx).*(F.*dGy - dFy.*G));
51    yn = y - (1./(dFx.*dGy - dFy.*dGx).*(-F.*dGx + dFx.*G));

      % Find the maximum difference between the new and original ...
         roots
      conv1 = max(abs((xn - x)));
      conv2 = max(abs((yn - y)));
56
      conv = max([conv1 conv2]);

      % Set the new permittivity and permeability guesses
      x = xn;
61    y = yn;

      % Calculate the new deltas
      dy = y + delta;
      dx = x + delta;
66
      k = k + 1;
   end

  % Pass out the relative permittivites and permeabilities
71 epsilon = y;
  mu = x;
```

Bibliography

1. Baker-Jarvis, J. *Measuring the Permittivity and Permeability of Lossy Materials: Solids, Liquids, Metals, Building Materials, and Negative-Index Materials.* Technical Report 1536, National Institute of Standards and Technology, February 2005.

2. Balanis, C. *Advanced Engineering Electromagnetics.* John Wiley & Sons, Inc., 1989.

3. Davidson, A., E. Strid, and K. Jones. "Achieving Greater On-Wafer S-Parameter Accuracy with the LRM Calibration Technique", 1989.

4. Gagnon, N. *Design and Study of a Free-Space Quasi-Optical Measurement System.* Master's thesis, University of Ottawa, 2002.

5. Gagnon, N., J. Shaker, P. Berini, L. Roy, and A. Petosa. "Material Characterization Using a Quasi-Optical Measurement System". *IEEE Transactions on Instrumentation and Measurement*, 52(2):333–336, April 2003.

6. Ghodgaonkar, D. K., V. V. Varadan, and V. K. Varadan. "Free-Space Measurement of Complex Permittivity and Complex Permeability of Magnetic Materials at Microwave Frequencies". *IEEE Trans. Instrum. Meas.*, 39(2):387–394, April 1990.

7. GTRC. *Users Guide: Theory and Operation of the GTRI Focused Beam System*, 2007.

8. Havrilla, M. *Class Notes Distributed in EENG 624: Electromagnetic Characteristics of Materials.* Graduate School of Engineering and Management, Air Force Institute of Technology, Wright-Patterson AFB OH, May 2009.

9. Havrilla, M. "Stripline Calibration". *Material Measurement Working Group Conference, AFRL, WPAFB OH*, 2009.

10. Hewlett-Packard. *Aplying the HP 8510 TRL Calibration for Non-Coaxial Measurements*, October 1987. 8510-8A.

11. Johnk, R. T., S. Tofani, and M. Kanda. "Time-Domain Measurements of the Electromagnetic Backscatter of Pyramidal Absorbers and Metallic Plates". *IEEE Transactions on Electromagnetic Compatibility*, 35(4):1381–1385, November 1993.

12. Johnson, L. and R. Riess. *Numerical Analysis.* Addison-Wesley, Reading, MA, 2nd edition, 1982.

13. Kaw, Autar. "Newton-Raphson Method of Solving Nonlinear Equations". Http://numericalmethods.eng.usf.edu.

14. Knott, E., J. Shaeffer, and M. Tuley. *Elements of Electromagnetics.* Scitech Publishing, Inc., 2nd edition, 2004.

15. Le Bras, J. L., M. Le Goff, B. Deschamps, A. Peden, D. Bourreau, and S. Toutain. "Quasi-Optical Circuit Measurement Method in W band". *in Proc. ESA Workshop Millimetre Wave Tech. and Applicat.*, 453–457, May 1998.

16. Le Bras, J. L., M. Le Goff, B. Deschamps, A. Peden, D. Bourreau, and S. Toutain. "Ka Band Quasi Optical Test Bench Using Focusing Horns". *Proc. 29th Europ. Microwave Conf. (EuMC)*, 2:240–243, October 1999.

17. Le Goff, M., J. L. Le Bras, B. Deschamps, D. Bourreau, A. Peden, and S. Toutain. "Focusing Horn Design for Wide Band Quasi Optical Circuit Measurements Without Time-Gating". *Proc. ESA Workshop Millimetre Wave Tech. and Applicat.*, May 1998.

18. McGuirk, J., M. Havrilla, P. Collins, and G. Hilderbrand. "A three-short focused beam calibration technique for material characterization measurements". *Antenna Measurement Techniques Association (AMTA) Conference Proceedings*, 122–126. Department of Operational Sciences, Air Force Institute of Technology, Wright-Patterson AFB, OH 45433, United States, St. Louis, Mo, November 2007.

19. Musil, J. and F. Zacek. "Microwave Measurements of Complex Permittivity by Free Space Methods and their Applications". *Amsterdam: Elsevier*. 1986.

20. Nicolson, A. M. and G. F. Ross. "Measurement of the intrinsic properties of materials by time-domain techniques". *IEEE Trans. Instrum. Meas.*, IM-19(4):377–382, November 1970.

21. Sadiku, M. N. O. *Elements of Electromagnetics*. Oxford University Press, Inc., 2001.

22. Technologies, Agilent. *Network Analyzer Basics*, 2004.

REPORT DOCUMENTATION PAGE

Form Approved
OMB No. 0704–0188

1. REPORT DATE *(DD–MM–YYYY)*	2. REPORT TYPE	3. DATES COVERED *(From — To)*
25–Mar–2010	Master's Thesis	Sept 2008 — Mar 2010

4. TITLE AND SUBTITLE

Application of the Three Short Calibration Technique in a Low Frequency Focus Beam System

5a. CONTRACT NUMBER

5b. GRANT NUMBER

5c. PROGRAM ELEMENT NUMBER

6. AUTHOR(S)

William E. Gunn Jr., 2d Lt, USAF

5d. PROJECT NUMBER

JON#10-134

5e. TASK NUMBER

5f. WORK UNIT NUMBER

7. PERFORMING ORGANIZATION NAME(S) AND ADDRESS(ES)

Air Force Institute of Technology
Graduate School of Engineering and Management (AFIT/EN)
2950 Hobson Way
WPAFB OH 45433-7765

8. PERFORMING ORGANIZATION REPORT NUMBER

AFIT/GE/ENG/10-10

9. SPONSORING / MONITORING AGENCY NAME(S) AND ADDRESS(ES)

Air Force Research Lab (Mr. Garrett Stenholm)
2591 K Street, Bldg. 254
WPAFB, OH 45433-7602
((937)-255-9179 Garrett.Stenholm@wpafb.af.mil)

10. SPONSOR/MONITOR'S ACRONYM(S)

AFRL/RYS

11. SPONSOR/MONITOR'S REPORT NUMBER(S)

12. DISTRIBUTION / AVAILABILITY STATEMENT

Approval for public release; distribution is unlimited.

13. SUPPLEMENTARY NOTES

14. ABSTRACT

Electromagnetic material characterization is the process of determining the constitutive parameters of matter. In simple media, these parameters are permittivity and permeability. Characterization of these values is often accomplished through the use of waveguides, transmission lines, coaxial cables, and resonant cavities. Free space measurements systems are employed since they are non destructive (i.e., no sample machining is required) and broadband. Traditionally, time domain gating is utilized to mitigate systematic errors. However, an artifact of this calibration technique is band edge corruption due to data windowing. The goal of this research is to develop and apply a Three Short Calibration Technique to the General Electric Low Frequency (0.5-2GHz) Focus Beam System in order to preserve band edge data. It is shown that when working with low frequencies, such as the focus of this research, coupling effects due to multiple bounces within the collimating and focusing lenses as well as lens-sample interaction are not easily calibrated out. Although the coupling effects introduce extraneous clutter into the extracted constitutive parameter values, the results obtained agree with the known reference values of tested dielectric samples. It is concluded that with a more in depth study in sample/lens interaction at low frequencies, this calibration technique could prove useful in the accurate extraction of the desired low frequency constitutive parameter values.

15. SUBJECT TERMS

material measurement, free-space, focus beam, frequency domain calibration

16. SECURITY CLASSIFICATION OF:			17. LIMITATION OF ABSTRACT	18. NUMBER OF PAGES	19a. NAME OF RESPONSIBLE PERSON
a. REPORT	b. ABSTRACT	c. THIS PAGE			Dr. Michael Havrilla
U	U	U	UU	85	**19b. TELEPHONE NUMBER** *(include area code)* (937) 785–3636, ext 4582; michael.havrilla afit.edu

Standard Form 298 (Rev. 8–98)
Prescribed by ANSI Std. Z39.18